DOI: 10.1002/adom.201700368

Article type: Review

Engineering Light at the Nanoscale: Structural Color Filters and Broadband Perfect Absorbers

*Chengang Ji, Kyu-Tae Lee, Ting Xu, Jing Zhou, Hui Joon Park, and L. Jay Guo**

C. Ji, Dr. K.-T. Lee, Prof. L. J. Guo

Department of Electrical Engineering and Computer Science, The University of Michigan, Ann Arbor, Michigan 48109, USA

E-mail: guo@umich.edu

Prof. T. Xu

National Laboratory of Solid State Microstructures, College of Engineering and Applied Sciences and Collaboration Innovation Center of Advanced Microstructures, Nanjing University, 22 Hankou Road, Nanjing 210093, China

Dr. J. Zhou

National Laboratory for Infrared Physics, Shanghai Institute of Technical Physics, Chinese Academy of Sciences, 500 Yutian Road, Shanghai 200083, P. R. China

Prof. H. J. Park

Submitted to ADVANCED OPTICAL MATERIALS

Department of Energy Systems Research, Ajou University, Suwon 16499, South Korea

Department of Electrical and Computer Engineering, Ajou University, Suwon 18499, South Korea

Keywords: structural colors, optical filters, broadband absorption, perfect absorbers, nanostructures

Recent advances in fabrication and processing methods have spurred many breakthroughs in the field of nanostructures that provide novel ways of manipulating light interaction on a well controllable manner, thereby enabling a wide variety of innovative applications. Structural colors have shown great promise as an alternative for the existing colorant-based filters due to their noticeable advantages, which open up diverse potential applications such as energy-efficient displays, ultrahigh-resolution imaging, ultrahigh-sensitivity biosensors, and building-integrated photovoltaics. Broadband perfect absorbers, which exploit extraordinary optical phenomena at subwavelength scale, have also received increasing attention due to their capabilities of improving efficiency and performance characteristics of various applications including thermoelectrics, invisibility, solar-thermal-energy harvesting, and imaging. This review highlights some recent progress in these two related fields. Structural colors based on optical resonances in thin-film structures, guided-mode resonances in slab waveguide gratings, and surface plasmon resonances (SPRs) in plasmonic nanoresonators are described. Representative achievements associated with broadband perfect absorbers, which include schemes employing highly absorbing media, multi-cavity resonances, and broadband impedance matching are investigated.

1. Introduction

Nanostructures exploiting either photonic or plasmonic resonances provide new optical properties and enable unique optical devices with desired functionalities.[1–8] Such novel characteristics offer great potentials for a wide variety of research fields such as near-field probes with ultrahigh resolutions for sensing and imaging, optical trapping at the nanoscale with

extraordinary precision, tight light confinement to deep subwavelength volumes via plasmonic lenses, and steering light beyond the diffraction limit. One emerging area that attracts much attention in recent years is the ability of designed nanostructures to generate distinctive colors employing optical resonant properties, often referred as structural colors. In contrast with the traditional approach of using different organic dyes or inorganic pigments to create colors, different structural colors can be created by using the same materials (e.g., metal and dielectric) but simply changing the geometry and dimension of the structures. Vivid structural colors can be observed in nature, e.g., Morpho butterfly wings, peacock feathers, fruits, beetles, and opals, arise from optical interference effects in multilayer structures.[9–14] Both transmissive or reflective colors have been realized by various means, offering distinct advantages such as high stability, high reproducibility, easy manufacturability, high spatial resolution, and slim dimension, over existing color filters that made of organic dyes or pigments to absorb a spectral portion in the visible wavelength range for the color generation.

Black can be considered as a special color, which can be created with nanostructured absorbers featuring highly-efficient and broadband absorption, or with overlapped absorption bands to cover the entire visible range. Broadband absorbers contrast the aforementioned color filters whose function is to produce a relatively sharp resonance to filter a narrow spectral range of visible light. Much effort was aimed at achieving “perfect absorption”, which can benefit various applications such as photovoltaics, solarthermal harvesting, photodetectors, thermal emitters, and bolometers, owing to their exceptional absorption characteristics with unique functionalities for energy harvesting and conversion.[3,15-34]

In this review article, the recent results of the structural color filters and the broadband perfect absorbers based on optical properties in the nanostructures, are discussed. The structural colors that exploit strong optical interference effects in thin-film nanostructures, waveguide-mode resonances, and surface plasmon resonances are described. Moreover, the broadband perfect absorbers utilizing broad optical resonances with highly absorbing media, multiple resonances, and broadband impedance matching, are investigated. Many methodologies can be extended to other wavelength ranges. We also provide an overview of their applications including solar energy harvesting, anti-counterfeiting, color printing, and light/thermal emitters.

2. Structural Color Filters

2.1. Fabry–Pérot Resonances

One of the simplest methods to create structural colors is based upon the Fabry-Pérot (F–P) resonances in thin-film structure comprising two metallic mirrors separated by an optically transparent dielectric medium. Constructive interferences take place in a transparent cavity layer at a certain wavelength, leading to a transmission peak for optical thin bottom metallic layer, or reflection valley for opaque bottom metal layer. F–P filters have been used to selectively transmit or reflect a certain portion of visible light by controlling the thickness of the cavity medium.[35–44] For displays, imaging, and color printing applications,[45] it is important to achieve angle-insensitive colors, which cannot be achieved with ordinary F–P cavities where the resonance shifts toward shorter wavelength with increasing angles of incidence. In order to mitigate the dependence of

optical properties on angles of incidence, reduced refraction into the structure by using materials with high refractive index, strong interference effects in highly absorbing media-based nanocavities, phase compensation, and localized resonances in metallic plasmonic nanostructures have been studied.[46–58] Here we use a reflective color design to illustrate the principle. **Figure 1a** depicts the schematic configuration that exploits the F–P resonances. Silicon nitride (Si_3N_4) and silver (Ag) are used as the cavity medium and the reflecting mirrors. Ag has been widely selected as the metallic mirror in the structural color filter designs as it has the lowest absorption losses at visible frequencies. By choosing the proper cavity length *d* to make the F–P interference resonance occur at wavelengths corresponding to red, green or blue colors, their complementary colors of cyan, magenta or yellow (CMY) can be readily obtained in the reflected light. Figure 1b shows the experimentally measured reflection spectra for the fabricated CMY filters with different Si_3N_4 thicknesses (C: 108 nm, M: 80nm, and Y: 54nm) while the same thicknesses for both the top (20 nm) and bottom (150 nm) Ag layers. The scanning electron microscopy (SEM) image of a device is shown in Figure 1c.

To mitigate the angle dependent properties of the F–P color filter, we analyze the angle dependence of a standard F–P etalon structure, as shown in Figure 1d. Here the refractive index of the dielectric layer is *n*, and the incident angle from air and refraction angle into dielectric layer is θ_1 and θ_2, respectively. For simplicity, we neglected absorption and material dispersion, but, as we will see later, the same principles apply if they are included. The reflectivity R_{FP} of the F–P etalon can be approximated as[59]

$$R_{FP} = \frac{2R \cdot (1 - \cos\delta)}{1 + R^2 - 2R\cos\delta}, \qquad (1)$$

where *R* is the reflectivity of the Ag film, δ is the phase difference between each succeeding reflection R_1 and R_2 and is given by

$$\delta = (\frac{2\pi}{\lambda}) \cdot n \cdot 2d \cdot \cos\theta_2 . \quad (2)$$

Reflection minima occurs at the resonant wavelength λ_r when the phase difference $\delta = 2m\pi$. Here we only consider the case of *m* = 1 because the other resonance modes are sufficiently separated from it and located in the near-infrared band. According to Snell's law $\sin\theta_1 = n\sin\theta_2$, we can get the resonance condition as $\lambda_r = 2d\sqrt{n^2 - \sin^2\theta_1}$.Then the variation of the resonant wavelength with incident angle θ_1 can be calculated as

$$\left|\frac{\Delta\lambda_r}{\Delta\theta_1}\right| \approx \frac{2d \cdot \sin\theta_1 \cdot \cos\theta_1}{\sqrt{n^2 \sin^2\theta_1}} . \quad (3)$$

Clearly the variation of the resonant wavelength is inversely proportional to the refractive index of the dielectric layer. Therefore a high-index dielectric cavity layer can lead to color filters with a smaller angle-dependence. Figure 1e shows the simulation and experiment results of the resonant wavelength variation with different incident angles. Here we employ silicon dioxide (SiO_2, $n \approx 1.46$), Si_3N_4 ($n \approx 2.0$), and zinc selenide (ZnSe, $n \approx 2.6$) for the dielectric cavity. For better comparison, the thickness of the dielectric cavity for each of the three materials is about 130 nm, 80 nm and 55 nm, respectively, to ensure the resonant wavelength for all three filters is around 550 nm. We can clearly see from Figure 1e that the device with a ZnSe dielectric cavity has the best performance in minimizing angle-dependent resonant wavelength variation, as expected from above analysis. Even

when the incident angle approaches 80°, the variation of the resonant wavelength is still less than 8% at λ_r = 550 nm. This small shift of the resonant wavelength would not cause a significant change in color perception. In comparison, the device with a SiO_2 dielectric cavity has strong angle-dependence. To confirm the simulated results, reflection spectra were measured from fabricated samples with angles of 20°, 40°, and 60°. The colored dots in Figure 1e represent the peak absorption measured at each angle and all data agree well with the simulation results. Figure 1g–h show the optical images of the fabricated CMY filters with ZnSe dielectric cavity at different reflection angles. Here the ZnSe cavity length for CMY color is about 75 nm, 55 nm and 40 nm, respectively, and CMY colors are almost invariable with incident angles.

The angle-insensitivity of the resonance will improve further with increased refactive index and reduced cavity thickness. However, increased index (*n*) is typically accompanied with increased optical loss (*k*). On the other hand, optical interference effects in highly absorbing media-based nanocavity has been studied by several groups, where non-trivial reflection phase shifts (i.e., not 0 or π) occur at the interface between the metal and the lossy medium, leading to the high angular tolerant performance that is ascribed to a special phase cancellation mechanism.[50–54] **Figure 2**a presents a schematic representation of an angular invariant visible wavelength filter consisting of an ultrathin semiconductor layer (amorphous silicon (a-Si)) sandwiched by two optically thin metal layers (Ag, 18 nm) on a glass substrate. The phase acquired upon the reflection at the metal (air)-semiconductor interface is significantly greater than π (reflection coefficient is a complex number), therefore unlike the case of lossless meidum, the F–P resonance condition can be satisfied for cavity thickness that is markedly thinner than the wavelength of the light in the medium. Based on the F–P cavity effects, red, green and blue (RGB) colors can be generated by simply varying the thickness of

a-Si (B: 9 nm, G: 15 nm, and R: 28 nm). Due to the fact that the ultrathin cavity thickness leads to the small change in the propagation phase shift with angle of incidence, which is almost completely cancelled by the non-trivial reflection phase shifts at the a-Si and Ag interfaces (Figure 2b–d), the designed color filters present great angular insensitivity up to 70° for all colors as displayed in Figure 2e – (j). Furthermore, since the device structure described above uses the semiconductor layer and has both top and bottom metallic layers that can be potentially employed as an electrode, the structure can be designed as optoelectronic devices to achieve dual-functionalities, thus opening up interesting possibilities of wavelength-selective photodetectors, and colored, semitransparent power-generating panels for building-integrated photovoltaics and energy-saving display technologies.[42,60–68] As one example, we have created colored solar cells by modifying the structure to allow asymmetric charge transport, using vanadium pentoxide (V_2O_5) adjacent to the a-Si to extract photo-generated holes, and indene-C_{60} bisad-duct (ICBA) on the opposite side of a-Si to transport electrons, as can be seen from the schematic diagram in **Figure 3**a. The effective refractive index of the cavity medium is primarily determined by the a-Si layer since it has a higher refractive index value than V_2O_5 and ICBA in the visible wavelength range. The spectral transmittance curves of the fabricated colored, semitransparent solar cells and the corresponding photographs showing distinctive RGB transmissive colors are provided in Figure 3b. Although the light absorption in the photoactive layer was limited by the ultrathin thickness, the solar cell performance characteristics with vivid semitransparent colors were achieved with ≈2% of the power conversion efficiency from the solar cells with 11 nm-thick a-Si layer, as presented in Figure 3c. Reflective colored solar cells were made based on similar principle empoloying opaque bottom metal layer,[60] and the traditional

F–P cavity where an optically transparent material is used as a cavity medium has also been integrated with the solar cell devices.[38,62,69,70]

It should be noted that because a-Si strongly absorbs the shorter wavelengths due to its bandgap, the M/a-Si/M structure cannot produce high effeciency color filters for shorter wavelength ranges. To address these challenges, it has been demonstrated that either an omnidirectional resonance in a MIM microcavity configuration or a phase compensating dielectric overlay integrated with the MIM cavity is exploited to achieve the angle-insensitive characteristics without sacrificing the efficiency for all the primary reflective and transmissive colors.[43,44,55,56,71] The lateral size of F–P cavity based color pixels should be greater than the optical wavelength to ensure proper operation, therefore imposing a spatial resolution that may have some impacts on applications in displays, security labels, and optical data storages. In addition to the limited spatial resolution, to fabricate colored pixels, the thickness of the inner cavity medium needs to be altered to tune the colors, which require separate lithographic and film deposition steps to produce the RGB colors in pixel units. To simplify the process, it is necessary to develop a new strategy that can address the aforementioned issues at the same time.

Recently, the structural color filters based on the strong resonance behaviors in an ultrathin semiconductor layer patterned at the subwavelength scale by using nanoimprint lithography over large areas as illustrated in **Figure 4**a were demonstrated.[72] The change in the linewidth of the subwavelength gratings at the fixed semiconductor thickness (t = 35 nm) leads to varied effective refractive index of the cavity medium for different reflective color generation, thereby creating the individual color pixels via one-step lithographic process. CMY reflective colors were produced from the nanostructures with the linewidth (C: 250 nm, M: 120 nm, and Y: 50 nm) and period (C: 420 nm,

M: 280 nm, and Y: 220 nm) of the nanogratings, respectively. Figure 4b–d present top-view and tilted-angle SEM images of the fabricated structural color filters, clearly exhibiting the well-defined dimension of the subwavelength gratings with a smooth sidewall. As the fundamental principle is based on the strong optical interference behaviors in the effective cavity where the ultrathin highly absorbing media are utilized, the angle dependent properties were greatly improved as can be seen from both simulated angle-resolved reflection spectra in Figure 4e–g and measured results in Figure 4h–j.

2.2. Guided-Mode Resonances

Guided-mode resonance (GMR) or waveguide-mode resonance is also oftenly used to produce narrow band resonances and its operation details are provided.[73–92] The GMR based color filters feature high color purity with high efficiency, especially when the structure does not involve light absorbing materials. **Figure 5**a depicts the schematic diagram of the GMR-based reflective structural color filters consisting of an array of the Si_3N_4 nanogratings patterned on a thin Si_3N_4 waveguide layer on a glass, where d_g, d_h, F, and Λ represent grating height, waveguide layer thickness, fill factor and period of the subwavelength gratings, respectively. Incident light is coupled into a leaky waveguide mode by the grating structure through the diffraction, which is enabled by satisfying the phase-matching condition. Then, the waveguide resonant mode is coupled out to the incident medium by the scattering, resulting in 100% of reflectance with a very narrow bandwidth at the resonant wavelength. In this study, the period of the grating structure was designed to be much smaller than the wavelength of visible light, yielding only a zero-order diffraction mode. Figure 5b

displays optical images of the fabricated GMR-based color filters presenting the reflective RGB colors. Figure 5c,d show simulated and measured spectral reflectance curves at normal incidence for s-polarization (i.e., electric field is parallel to the direction of the subwavelength gratings), clearly the efficiency of such dielectric GMR based has very high efficiency due to the absence of light absorbing materials. It has been demonstrated that the metallic nanogratings can also be employed to create the transmission RGB colors in the GMR-based structural color filters.[81,82] As exemplified in Figure 5e, the metallic resonance waveguide grating structures consist of two dielectrics deposited on the glass substrate. The triple layer forms the effective waveguide with sub-wavelength Ag gratings providing extra momentum for coupling incident light into a waveguide resonant mode at a certain frequency (Figure 5f). Note that the center wavelengths in the visible range and hence the resulting colors can also be shifted by varying the refractive index, thickness and angles of incidence. Although the GMRs provide a sharp resonance with the very narrow bandwidth, it is difficult to highly suppress the off-resonant wavelength components, which are critical to attain the enhanced color purity. Additionally, the optical properties of the GMRs are highly dependent on the incident angles, which could be mitigated by several methods.[93–96]

2.3. Surface Plasmon Resonances

Plasmonic nanostructures have generated much interest with the development of recent nanofabrication methods and capabilities of optical field localizations into subwavelength dimensions. The plasmonic nanostructures have also shown great promise for the structural colors.[65,71,97–122] The early demonstration of extraordinary optical transmissions through a hole

array periodically perforated on a thin metal film can be considered as the first example.[123] Recently, plasmonic color printing with the subwavelength resolution has become a flurishing area, dramatically enhancing printing resolutions to ≈100 000 dots per inch (dpi).[57,101,108,111]

An example of the plasmonic color filter structures consisting of an array of the subwavelength gratings in the MIM nanocavity configuration on a transparent substrate is schematically shown in **Figure 6**a. Two 40 nm-thick aluminum (Al) mirrors, separated by a 100 nm-thick ZnSe dielectric film, the structure exploits the coupled surface plasmon modes at the two Ag/ZeSe interfaces (dispersion shown in Figure 6b), especially the assymetric mode shows a linear dependence of frequency v.s. wavevector (red line in Figure 6b). When periodic nanogroves are introduced, light incident upon the structure from the substrate side can be coupled to the plasmon waveguide modes via grating coupling. The confined plasmon waveguide resonant modes are then efficiently converted to the propagating waves by scattering with the help of the top Al nanogratings, thereby transmitting a certain spectral range to the far field in the forward direction. Figure 6b depicts the plasmon dispersion of the MIM stack array for p-polarization where an oscillating direction of electric field is perpendicular to the direction of the subwavelength gratings. Figure 6c presents the simulated spectral transmittance curves of the plasmonic transmissive structural RGB colors, obtained with the stack period of 360, 270, and 230 nm, respectively. In Figure 6d, the cross-sectional view of the simulated time-average magnetic field intensity distribution and electric displacement profiles (red arrow) into the MIM stack at 650 nm for p-polarization is described. It is obvious that incident light is efficiently coupled into the antisymmetric waveguide modes with strong magnetic response. Figure 6e provides measured transmission spectra of the fabricated plasmonic color filters under s- (triangles) and p-polarized light (circles) illuminations, clearly exhibiting strong polarization

dependent spectral properties. The devices show dual-functionalities, where it creates the RGB transmissive colors as well as p-polarized light transmission. Figure 6f illustrates micrographs of the fabricated plasmonic color filters with the different stack period from 200 to 360 nm.

Both GMRs and SPRs are highly sensitive with respect to the angles of incidence. Though not desirable for displays, such properties can be exploited for angle-sensitive pixels in image sensors, angle-selective biochemical sensors, solar and thermal energy harvesting, and anticounterfeiting technologies.[87,124–127] In particular for the anticounterfeiting application, although color-changing inks, fluorescent dyes, and magnetic inks have been widely used for holograms and watermarks in both passports and checks, the angle-sensitive structural colors can also be employed for the anticounterfeiting applications as an additional security feature that is difficult to replicate with traditional means.[87,116]

Next, some strategies to diminish the angle-sensitive characteristics, which rely on either localized resonances in deep subwavelength nanogrooves through light funneling or localized surface plasmon resonances (LSPRs) in the ultrathin metallic nanopatch array, are described.

Figure 7a depicts the schematic diagram of the metallic nanocavity-based wide-angle reflective structural color filters consisting of dielectric subwavelength gratings that is conformally covered by Ag, and the corresponding SEM image. The plasmonic structures were designed, where incident light is tightly confined into the deep subwavelength grooves by light funneling instead of grating-based coupling of light into the SPRs. Figure 7b displays how light is redirected into the nanogrooves by the light funneling effect, along with the induced polarization charge and Poynting vector distribution. In Figure 7c, simulated (solid lines) and measured (dashed lines) spectral reflectance curves of the

fabricated structures with different depth of the subwavelength grooves at normal incidence are provided. At the resonant wavelength, incident light is strongly concentrated into the nanogrooves and eventually absorbed by the metallic layer, thus producing reflective CMY colors. Figure 7d,e describe measured angle-resolved reflection spectra with different depth of the structures at the fixed period (180 nm) and linewidth (50 nm), apparently exhibiting that the resonances remain nearly constant over a broad range of incident angles up to 75° due to the localized characteristic of the resonance. Such strong field confinement could be adopted by a wide range of applications such as optical data storage with ultrahigh resolution, plasmonic emitters and chemical/bio sensors with ultrahigh sensitivity. It has also been shown that the LSPRs in an array of the ultrathin patch patterned in a single metallic layer enable the color generation with angle-insensitive performance. Figure 7f describes the schematic drawing of the LSPRs-based angle robust ultrathin structural color filters on a transparent substrate, thus being able to generate both reflective and transmissive colors at the same time. The reflective RGB colors and the corresponding transmissive CMY colors are produced by varying the duty ratio of the structure. 70, 140, and 240 nm of the period with the fixed thickness of the metal patch array at 20 nm were used for the reflective RGB colors, respectively. Simulated angle-resolved transmission spectra for the yellow and magenta colors are given in Figure 7g,h, respectively. As is seen from the figures, the resonances are almost maintained at the same wavelengths with increasing the angles of incidence up to 60°.

One interesting capability of the plasmonic color filters is to print the colors with the deep-subwavelength resolution that can even beyond the diffraction limit, which is ascribed to their unique ability of localizing light into a small sub-diffraction volume.[57,101,108,111,128,129] **Figure 8**a provides the schematic representation of the two plasmonic nano-pixels, where each pixel

comprises four nano disks. The pixels support particle resonances whose scattering strength was increased by a metal back-reflector so that different colors are able to be reflected without varying the periodicity of the plasmonic nanostructures. Figure 8b presents optical micrographs of 50 × 50 mm square Lena image, where the pixel was a 250 × 250 nm square, before and after a deposition of the metal layers. A laser post-writing method was also utilized for printing colors on prefabricated plasmonic metasurfaces with the sub-diffraction-limit resolution of 127 000 dpi over large areas as presented in Figure 8c andd.[128] Morphological changes of the prefabricated metasurfaces were enabled by generating transient local heat at a single unit cell level by the laser pulses, which can vary the resonant wavelength of the SPR and hence create the different color appearances.

Although various nanostructures described above were fabricated via top-down nanofabrication techniques such as electron-beam lithography, laser interference lithography, nanoimprinting lithography and focus ion beam technology, there have also been reports on achieving these schemes through bottom-up nanofabrication approaches such as colloidal self-assembly fabrication, metal dewetting method and electrochemistry technique.[111,130–132] Such bottom-up fabrication methods start from small building blocks such as atoms, molecules, nanoparticles and clusters, which can be assembled in a well-arranged manner to build the nanostructures. **Figure 9**a presents a fabrication process flow of the wide-gamut plasmonic color surfaces via a colloidal self-assembly over large area. A monolayer of polystyrene (PS) nanospheres was self-assembled and transferred onto a polymer film, which then utilized as a mask to pattern the nanostructures, where the diameter of the PS nanospheres was controlled by using reactive-ion etching (RIE). Figure 9b shows the SEM and the corresponding micrographs of the fabricated plasmonic color patterns, displaying vivid colors that can be varied by altering the pitch (*P*), height (*H*), radius (*R*) and inner radius (*r*) of

the nanopatterns. Figure 9c,d exhibit the SEM and the corresponding optical images of the fabricated structural colors achieved from dewetted nanoparticle arrays and ultrathin metallic films with different thicknesses of a metal film. The metal dewetting on a glass substrate enables a formation of nanocaps of a variety of shapes and sizes, which can create vibrant transmission and reflection colors. These bottom-up approaches are advantageous in producing vivid colors with improved morphological quality and uniformity, and at low cost over large area.

As a summary, we have compared the performance of structural color filters, which includes brightness, angular sensitivity, spatial resolution, and fabrication cost, employing those three different mechanisms discussed above in **Table 1**.

3. Broadband Perfect Absorbers

In contrast to the aforementioned structural color filters where a sharp resonance with capabilities of filtering a narrow spectral range of visible light is highly desired for producing the colors with high purity, nanostructured 'perfect black', which can be regarded as a special color featuring highly-efficient and broadband absorption at the visible frequency, has also attracted substantial interest in different research fields.

Although we primarily focus on the broadband absorbers in this review, there have also been previous works achieving narrow band absorption characteristics, which are relevant to applications such as nanoantennas, selective thermal emitters, and sensing.[133–137]

Numerous approaches have been developed for achieving the perfect absorption. The one-dimensional (1D) MIM stack, which was firstly described by Salisbury for radar wave absorption dating back to 1952, provides the simplest solution.[138] The absorption is significantly enhanced at the resonant frequency due to the accumulated electric field inside the effective F–P cavity.[35,71,139–141] With the advent of various advanced nano-fabrication technologies, plasmonic structures have emerged as appealing alternatives for achieving strong absorption in metallic nanostructures patterned at the wavelength or subwavelength scale.[142–148] By exciting the SPRs via coupling of light to collective oscillations of electrons on the metal surface, light can be tightly trapped around the metals, and efficiently absorbed by the metal. More recently, metamaterials, which are artificially constructed materials exhibiting unusual electromagnetic characteristics that are not possible with natural materials, have been geometrically engineered to attain perfect absorption at various frequency regimes.[134,142–144,149–151] However, the resulting resonances intrinsically present a narrow spectral coverage, thus dramatically limiting numerous potential applications. The most straightforward way to broaden the absorption is to involve highly absorbing materials into those structures, which essentially lowers the quality-factor (Q-factor) of the resonant cavities.[144,152–154]

The additionally incorporated resonators provide flexibility in selecting absorption frequency range and can achieve even broader absorption, but also require more complicated fabrications.[155–159] Novel structures featuring broadband impedance matching without exciting resonances have been recently proposed accompanied with various cost-effective fabrication methods, thereby opening up a new path to the extensive use of broadband absorbers in various applications.[160–162]

3.1. Broadband Absorption with Lossy Materials

It is self-evident that the absorption can be effectively broadened and intensified by employing materials that have high losses. Firstly demonstrated in the MIM F–P cavity, the broadband absorption feature can be easily achieved by replacing the noble metals (e.g., Ag, gold (Au), and copper (Cu)) with lossy ones (e.g., chromium (Cr), nickel (Ni), tungsten (W), and titanium (Ti)).[152,163–166] For instance, Li et al. proposed a broadband absorber with high efficiency comprising a simple tri-layer Cr/SiO_2/Cr configuration. Over ≈97% of the absorption efficiency averaged from 450 to 800 nm was achieved by using lossy metallic layers as a mirror for the F–P cavity. As illustrated in the inset of **Figure 10**a, the bottom metallic layer is optically thick to block any transmission (i.e., $A = 1 - R - T$ with A, R, and T referring to absorption, reflection, and transmission, respectively), and the optimized thickness (t) of the top Cr is found to be 3 nm that allows incident light to pass through the entire structure so that it provides a certain level of the reflection for the cavity effect while also offering sufficient light absorption, thereby remarkably enhancing the overall absorption efficiency. The “poor” F–P cavity effects indicated by the weak electrical field confinement as shown in Figure 10b, which features both low field intensity and large confinement area around the red color regime, as well as the inherently high loss of Cr result in the broadened while efficient absorption (peak absorption >99% at 560 nm) as presented in Figure 10a for the normal incidence. Resulting from the broadband behavior, the angular sensitive property is greatly mitigated for both p- and s-polarization light as is

seen from Figure 10c, which is highly desirable in diverse applications. It is noteworthy that the absorption performance can be further enhanced by incorporating an additional dielectric AR layer atop.[33,167,168]

Using lossy medium is also an effective way to make plasmonic structures and metamaterials into broadband absorbers. Ding et al. realized the broadband near infrared (NIR) via a MIM plasmonic metamaterial that exploited Ti as the top metallic patterns.[153] As depicted in **Figure 11**a, the structure consists of a 160 nm-thick SiO_2 layer sandwiched by a continuous Au substrate and an array of Ti disks (period (p) = 600 nm). Au is 100 nm-thick to avoid transmission, and the thickness and the diameter of the Ti disk are t_m = 30 nm and d = 400 nm, respectively. The absorption spectra in Figure 11b show that this new design with slight modifications exhibits broadband absorption properties over a wide range of wavelengths from 875 to 1840 nm with over 90% of efficiency. By plotting the electric and magnetic field distribution at the absorption peak 1468 nm (Figure 11e,h,j), the LSPRs, i.e., the guided plasmonic mode in typical MIM waveguides, is clearly observed between the Ti disk and Au substrate. The absorption around this resonance gets significantly broadened due to the high loss of Ti, which lowers the Q-factor of the waveguide cavity. To date, other refractory metals as Ti have also been demonstrated for broadband absorption and semiconductors such as silicon (Si) and germanium (Ge) can be included instead of transparent insulators for extra absorption improvement.[154,169–171] Interestingly, an additional propagating surface plasmon resonance (PSPR) excited at the short wavelength (Figure 11d,g,i) due to the relatively large Ti pattern period further boosted the absorption

as presented by the other absorption peak at 914 nm in Figure 11b. This indicates another way for metamaterials to attain broader absorption, i.e., exciting various resonances at different wavelengths simultaneously, which will be discussed in more detail in Section 3.2. As the refractory metals feature high melting points and high temperature durabilities, those efficient and broadband structures that exploit the refractory metals have opened new perspectives for thermophotovoltaics (TPVs).[32,172–174] However, since most of the absorption is resulting from the metallic loss, structures based on this method can be hardly used to enhance the photovoltaic (PV) performance.

3.2. Broadband Absorption Employing Multiple Resonances

In addition to utilizing lossy metals to broaden the absorption via the low-Q-factor cavity, alternative strategies have also been developed by integrating multiple resonators working at neighboring wavelengths together. As one example, Lee et al. created a broadband absorber at visible frequencies exploiting two stacks of a metal (Ag) and a semiconductor (a-Si) as shown in **Figure 12**a.[175] The second a-Si layer on the very top induces additional resonances (#1 @496 nm and #3 @591 nm) apart from the one inside the bottom a-Si (#2 @568 nm) as clearly presented by the spectrum of the electric field intensity in Figure 12b. As a result, the absorption, which is proportional to the electric field intensity, gets effectively expanded with the multiple absorption peaks (red curves in Figure 12c). Another type of ultra-broadband absorber is designed by subsequent deposition of ultrathin

semiconductor (Ge and a-Si) and dielectric (titanium dioxide (TiO_2) and magnesium floride (MgF_2)) layers on top of a thick lossy metal (Cr), with the relevant schematic shown in Figure 12d.[176] The absorption characterized by multiple peaks in Figure 12e ranges from 400 nm to 2 μm with the average efficiency of ≈97.76%, offering a practical method to broadband perfect absorbers. Highly efficient absorption property is ascribed to the AR effects induced by the graded refractive index profile (i.e., MgF_2 / TiO_2 / a-Si / Ge), while ultrabroadband absorption characteristics arise from the excitation of multiple resonances in each layer of the tandem structure comprising diverse absorptive materials. Figure 12f presents an optical image of the fabricated absorber taken at normal illumination, showing a totally black appearance. Considering both designs described above already involve semiconductor media, they can be potentially applied to PV cells by inserting efficient hole and electron transporting layers, and using a transparent electrode, such as indium tin oxide (ITO), on the top.

Significant efforts have been made to expand the absorption bandwidth of plasmonic structures and metamaterials via mixing multiple resonators within a single unit cell. Distinct from 1D layered configuration where additional cavities can only be accumulated vertically, those patterned structures allow for multiple resonances arranged along any directions in the 3D space, thus enabling design varieties and innovative effects.[155,156,169,177] **Figure 13**a shows a noble-metal-based MIM laminate with the top Ag layer patterned as crossed trapezoid arrays. In the configuration, top and bottom Ag layers are both 100 nm, the sandwiched SiO_2 has a thickness of 60 nm, and the periodicity is 300 nm. The gradually

varying width within each trapezoid cell allows for different localized resonances excited at each width along the trapezoid, thus enabling a decent extinction spectrum with the average efficiency of 71% between 400 and 700 nm (Figure 13b,c). As seen in the 2D absorption maps at three absorption peaks, light is absorbed at the centre position of the unit cell @475 nm (Figure 13e), below the narrow section of trapezoid array @560 nm (Figure 13f), and underneath the center of the y-directional trapezoid @630 nm (Figure 13g), respectively. Due to the crossed symmetric arrangement, the absorption response is also robust to the polarization as indicated by the similar results at two polarization angles (ϑ = 0° and 45°) in Figure 13b,c.

Generally, integrating different-sized resonators within a single unit, instead of using these irregularly shaped structures that are difficult for fabrication, is more frequently utilized for realizing multiple resonances, except for RF frequencies,[178] where the structures are large and easy to fabricate. For instance, Cui et al. successfully controlled absorption over a broad band in the IR regime with a horizontal array of multi-sized strip antennas, wherein each size within a unit cell corresponds to plasmonic MIM resonances at distinct wavelengths.[179] On the other hand, anisotropic metamaterials based on tapered, alternating metal-dielectric multilayered structures (i.e., vertical arrangement) have been subsequently adopted for broadband absorption in the microwave, IR, and visible ranges.[180–182] Incident light at different wavelengths will be captured at certain positions of the sawtooth shaped configuration, which can be equivalently treated as a hyperbolic matematerial waveguide with varying width, and consequently get absorbed.

Broadening the absorption via multiple resonators has also been extended to 3D metallic patches or nanoparticles (NPs) to eliminate the polarization dependence, where the latter provides a simple and cost-effective solution suitable for mass production.[169,183–186] A novel water desalination device based on plasmon-enhanced broadband absorber was experimentally demonstrated by Zhu and co-workers in 2016, which presented a great example of converting the solar radiation into the thermal energy.[187] As illustrated in **Figure 14**a, the structure can be easily fabricated by the self-assembly of Al NPs into a 3D nanoporous aluminum oxide membrane (AAM). Due to the hybridization of LSPRs and non-radiative plasmon decay, such Al NP-based plasmonic structures absorb a broad solar spectrum (>96%, Figure 14c) and lead to highly localized heating of water inside the deeply subwavelength volumes (Figure 14b), thus enabling efficient (≈90% energy transfer efficiency, Figure 14d) and effective solar desalination.

It is worth noting that various resonances induced by multi-sized resonators are essentially based on the same absorption principles in the above discussion. Specifically, the stacked resonances in the 1D layered structures are attributed to the same F–P cavity effects and the examples of metamaterials employ plasmonic waveguides despite of different widths to excite discrete absorption resonances. The broadband absorbers with multiple resonances have also been demonstrated by coalescence of various absorptive mechanisms. One good example is given in Ref. [188] adopting the square, ring-like Ni grating/SiO_2/Ni substrate configuration. With the well-optimized dimensions (i.e., 600 nm period, 400 nm-thick top Ni, 100 nm-thick SiO_2, 0.85 lateral filling ratio, and enough thick Ni substrate), >90% incident

light are absorbed by this modified MIM structure for both polarization from 300 to 1000 nm, wherein absorption effects at short (≈450 nm) and long (≈1000 nm) wavelengths are recognized as the cavity resonance within the hollow regime of the concave grating and magnetic polaritons (i.e., LSPRs), respectively. Considering the wide variety of effects that can absorb light, such as grating diffraction, waveguiding, F–P resonance, PSPRs, LSPRs, etc., this basic idea further enriches the broadband absorber designs so that can satisfy different requirements.[19,154,169,189–191] Although additional resonators allow flexibilities in selecting desired absorption band positions, most structured described above require delicate resonant cavities, which significantly increases the fabrication complexity, thereby hindering their practical applications.

3.3. Broadband Absorption by Impedance Matching (Non-Resonant Absorbers)

Composed of periodically or randomly arranged patterns on the subwavelength scale, metamaterials can be intuitively treated with effective materials. The corresponding effective electric permittivity (ε) and magnetic permeability (μ) are dependent on the geometrical dimensions. Typically, metamaterials are compact in size, which are highly desirable in nowadays high-density on-chip integration, and can be engineered to achieve many special properties that are impossible with natural materials. Facilitated by rapid advances in miro- and nano-fabrication technologies, metamaterials hold great promise in various areas, such as superlenses, electromagnetic cloaking, optical filters, perfect

absorbers, metamaterial antennas, etc.[101,129,149,192–194] Taking the advantage of the electric (ε) and magnetic (μ) responses that can be engineered, non-resonant broadband absorption (i.e., different from those resonant absorbers discussed above) is possible for metamaterials through impedance matching over a wide wavelength range by geometrically adjusting the structure.

Low density carbon nanotube (CNT) forest, which is an array of vertically aligned nanotubes with the typical diameter of ≈10 nm, the spacing of ≈50 nm, and the corresponding bulk density < 0.1 g cm^{-3}, is one of the most promising candidates for black materials based on the non-resonant impedance matching principle.[161,195–199] It possesses near unity refractive index with slight loss (i.e., $n_{eff} = 1 + i\delta$ with δ = 1) across a wide wavelength range retrieved by the effective medium theory (**Figure 15**d), which consequently can minimize the reflection due to the perfect impedance matching to the air and provide total absorption with sufficient thickness. SEM images of multi-walled CNT forest on a flat substrate grown by plasma-enhanced chemical vapor deposition (PECVD) are displayed in Figure 15a andb, presenting the sparseness and alignment properties of the material. After increasing the thickness from 6.5 to 70 µm, both the reflection and the transmission are efficiently suppressed (≈0.1%), thus achieving a near unity absorption over the whole visible range (Figure 15c). As a proof-of concept, an optical image of a “tank” pattern (fabricated by focused ion beam (FIB) milling) covered by CNT forest (SEM image in Figure 15e) was taken under broadband visible illumination, showing the perfect cloaking of the object (Figure

15f). Other works have further extended the perfect absorption capability of the CNT forest from UV to far-IR ranges and applied it as the black body of near-unit emissivity.[161] Based on the same mechanism, i.e., reaching near-unity effective refractive index by controlling material volume ratio, arrays of sharp patterns employing lossy media (e.g., Si nanocones, tungsten (W) pyramids) could also serve as a broadband absorber in the visible and NIR range.[21,160,162,200] Those structures featuring the graded transition of the effective refractive index, which is very close to air at the cone top, exhibit great AR effects, thus resulting in the overall absorption enhancement. Similarly enhanced absorption can be achieved if applying nano-patterned AR coatings of lossless dielectrics onto absorptive substrates.[23,201] So far, various methods have been developed for achieving those graded nano-structures, including ion bombardment, femtosecond laser texturization, and RIE, which extensively simplifies the fabrication and paves the way for PVs of high efficiencies.[21,160,162,202–205] For example, the PCE of a flat crystalline Si solar cell under AM1.5G illumination was improved from 8.7 to 13.1% (over 50% increase) as a result of applying Si nanocones as an AR layer onto the surface to improve the absorption and corresponding photo-current (J_{sc}).[206]

In addition, alternating metal-dielectric multilayered structure with an optical topological transition (OTT) provides another approach for wide band absorption.[207–211] Since each layer involved in this special structure here is much thinner than the wavelength, the whole system can be described as an effective anisotropic medium with the parallel ($\varepsilon_{\parallel}$) and

perpendicular ($\varepsilon_{\perp}$) permittivities, respectively. When the wavelength decreases across the epsilon-near-zero (ENZ, corresponding to $\varepsilon_{\parallel} = 0$) point, the layered structure changes from an effective metal to an effective dielectric for both polarizations, which is more impedance matching to surrounding air, thus allowing the light to penetrate into the structure and getting absorbed at all short wavelengths (compared to the ENZ frequency). Zhou et al. proposed a broadband absorber/emitter based on the OTT effect to improve thermal/light interconversion efficiency. **Figure 16**a depicts the schematic diagram of the multilayered structure employing titanium nitride (TiN) and SiO_2 as the metal and dielectric, respectively. By setting the ENZ point at the board between the visible and IR range through tuning the fill ratio of the metal as presented in Figure 16b, the IR emission is largely suppressed compared to that of W filament (Figure 16c), which effectively enhances the lighting efficiency featuring a visible/IR emission ratio of >0.6 (2.3 times higher than that of conventional incandescent lighting). It is worth noting that the high visible light absorption and low IR radiation of the OTT structure here make it also suitable for solar energy storage if integrated with heat engines.

Broadband absorbers employing impedance matching methods exhibit wide absorption bandwidth comparable to that based on multiple resonances, but can be realized via various cost-effective methods as discussed above. However, the number of designs based on this mechanism is very limited and more structures need to be exploited. As a summary, **Table 2**

has listed the advantages and disadvantages of each method discussed above for achieving broadband perfect absorption.

4. Summary and Outlook

We have reviewed various structural colors that exploit F–P resonances, GMRs, SPRs and LSPRs in diverse nanostructural configurations. The structural colors provide distinct advantages in terms of efficiency, dimension, durability, manufacturability, and resolution over the conventional color filters that rely on chemical pigments, thereby opening up many potential applications. The simplicity of the structural color designs leads to easy integration with electronic and optoelectronic devices.[42,63–65] In addition, the SPR-based structural colors introduce new capabilities of printing colors with deep-subwavelength resolution exceeding 10^5 dpi, thus allowing their implementation in a number of applications such as security marking, display and information storage. Many attempts have also been made toward the demonstration of dynamically tunable colors and scalable fabrications of the structural colors over large areas. However, it is still difficult to produce vivid colors with high efficiency and simultaneously high color purity as there is a trade-off between these two characteristics. This could be addressed by exploiting multi-cavity resonances in a transparent cavity medium, which has been recently demonstrated on a flexible substrate.[212] Although the angle-sensitive colors, which are obtained from the nanostructures where either GMRs or SPRs are exploited, hold great potential for hologram and anti-counterfeiting, the angle-insensitive features, which are highly desired in display, imaging and sensing, could be achieved by using high index media, phase cancellations and localized resonances. Intrinsic losses in metals result in poor Q-factor

and therefore degraded color vibrancy, which could be improved by employing new low-loss Al-doped Ag materials, and exploiting hybridization and Fano resonances.[213–217] With the rapid development of nanofabrications and optical materials, the structural colors can provide us with the distinct possibility to open up novel technologies, including optical data storage, chemical/bio sensing, and dynamically tunable display.

The broadband absorbers, which reply on a variety of strategies, have also been summarized. In light of the inexhaustible solar radiation from the sun every day, effectively integrating these broadband absorbers with the solar cells and confining the absorption inside the active layer to improve the PCE is of vital importance. Recently, enhancing the absorption in ultrathin films receives increasing interest since it can further boost the PV performance by effectively suppressing the carrier recombination.[50,52,175,218–223] Their absorption characteristics over a broad range of the wavelength show great promise in a variety of applications such as invisibility cloak, solar cells, light detection, and thermoelectric devices. For some research fields, including solar-thermal harvesting, anti-reflection coating, and imaging, the ultrabroadband absorption features are highly desired, which can be enabled by exploiting the multi-cavity resonances and broadband impedance matching. By making use of the high temperature durability of media such as refractory metals, the broadband absorbers can also be attained, which hold considerable potential in heat engines and thermophotovoltaic (TPVs). Instead of the multilayer thin-film structures, different patterns with 2D and 3D geometric configurations can also be incorporated in a single unit, which can provide the possibility of realizing the broadband absorption characteristics for mass production. Benefiting from different advanced micro- and nano-fabrication technologies increasingly emerged,[106,130,224–233] numerous novel concepts with attractive features have been proposed and subsequently realized,

opening up more opportunities for further advancement. We foresee a promising future for the artificial colors and broadband absorbers whose optical properties are determined by the structures, and many emerging applications.

Acknowledgements

C.J. and K.-T.L. contributed equally to this work. The authors acknowledge the support by the National Science Foundation (DMR 1120923, ECCS 1202046, CMMI-1635636) and Samsung. HJP acknowledges the support by the Ajou University research fund.

Received: ((will be filled in by the editorial staff))
Revised: ((will be filled in by the editorial staff))
Published online: ((will be filled in by the editorial staff))

[1] A. F. Koenderink, A. Alù, A. Polman, *Science* **2015**, *348*, 516.

[2] J. A. Schuller, E. S. Barnard, W. Cai, Y. C. Jun, J. S. White, M. L. Brongersma, *Nat. Mater.* **2010**, *9*, 193.

[3] H. A. Atwater, A. Polman, *Nat. Mater.* **2010**, *9*, 205.

[4] J. D. Caldwell, I. Vurgaftman, J. G. Tischler, O. J. Glembocki, J. C. Owrutsky, T. L. Reinecke, *Nat. Nanotechnol.* **2016**, *11*, 9.

[5] N. Meinzer, W. L. Barnes, I. R. Hooper, *Nat. Photonics* **2014**, *8*, 889.

[6] F. Xia, H. Wang, D. Xiao, M. Dubey, A. Ramasubramaniam, *Nat. Photonics* **2014**, *8*, 899.

[7] D. K. Gramotnev, S. I. Bozhevolnyi, *Nat. Photonics* **2010**, *4*, 83.

[8] Z. Fang, X. Zhu, *Adv. Mater.* **2013**, *25*, 3840.

[9] P. Vukusic, J. R. Sambles, C. R. Lawrence, *Nature* **2000**, *404*, 457.

[10] J. Zi, X. Yu, Y. Li, X. Hu, C. Xu, X. Wang, X. Liu, R. Fu, *Proc. Natl. Acad. Sci. USA* **2003**, *100*, 12576.

[11] P. Vukusic, J. R. Sambles, *Nature* **2003**, *424*, 852.

[12] S. Vignolini, P. J. Rudall, A. V. Rowland, A. Reed, E. Moyroud, R. B. Faden, J. J. Baumberg, B. J. Glover, U. Steiner, *Proc. Natl. Acad. Sci. USA* **2012**, *109*, 15712.

[13] B. R. Wasik, S. F. Liew, D. A. Lilien, A. J. Dinwiddie, H. Noh, H. Cao, A. Monteiro, *Proc. Natl. Acad. Sci. USA* **2014**, *111*, 12109.

[14] Y. Zhang, B. Dong, A. Chen, X. Liu, L. Shi, J. Zi, *Adv. Mater.* **2015**, *27*, 4719.

[15] P. Spinelli, V. E. Ferry, J. v. d. Groep, M. v. Lare, M. A. Verschuuren, R. E. I. Schropp, H. A. Atwater, A. Polman, *J. Opt.* **2012**, *14*, 024002.

[16] J. Zhu, Z. Yu, S. Fan, Y. Cui, *Mater. Sci. Eng., R* **2010**, *70*, 330.

[17] V. E. Ferry, M. A. Verschuuren, M. C. v. Lare, R. E. I. Schropp, H. A. Atwater, A. Polman, *Nano. Lett.* **2011**, *11*, 4239.

[18] V. E. Ferry, M. A. Verschuuren, H. B. T. Li, E. Verhagen, R. J. Walters, R. E. I. Schropp, H. A. Atwater, A. Polman, *Opt. Express* **2010**, *18*, A237.

[19] J. Zhu, C.-M. Hsu, Z. Yu, S. Fan, Y. Cui, *Nano. Lett.* **2010**, *10*, 1979.

[20] K. X. Wang, Z. Yu, V. Liu, Y. Cui, S. Fan, *Nano. Lett.* **2012**, *12*, 1616.

[21] S. Wang, B. D. Weil, Y. Li, K. X. Wang, E. Garnett, S. Fan, Y. Cui, *Nano. Lett.* **2013**, *13*, 4393.

[22] X. Chen, B. Jia, J. K. Saha, B. Cai, N. Stokes, Q. Qiao, Y. Wang, Z. Shi, M. Gu, *Nano. Lett.* **2012**, *12*, 2187.

[23] P. Pathi, A. Peer, R. Biswas, *Nanomaterials* **2017**, *7*, 17.

[24] W. Chihhui, N. Burton, III, J. Jeremy, M. Andrew, Z. Byron, S. Steve, S. Gennady, *J. Opt.* **2012**, *14*, 024005.

[25] L. Zhou, Y. Tan, D. Ji, B. Zhu, P. Zhang, J. Xu, Q. Gan, Z. Yu, J. Zhu, *Sci. Adv.* **2016**, *2*, e1501227.

[26] N. T. Panagiotopoulos, E. K. Diamanti, L. E. Koutsokeras, M. Baikousi, E. Kordatos, T. E. Matikas, D. Gournis, P. Patsalas, *ACS Nano* **2012**, *6*, 10475.

[27] X. Hu, W. Xu, L. Zhou, Y. Tan, Y. Wang, S. Zhu, J. Zhu, *Adv. Mater.* **2017**, *29*, 1604031.

[28] X. Li, W. Xu, M. Tang, L. Zhou, B. Zhu, S. Zhu, J. Zhu, *Proc. Natl. Acad. Sci. USA* **2016**, *113*, 13953.

[29] X. Hu, X. Zhang, L. Liang, J. Bao, S. Li, W. Yang, Y. Xie, *Adv. Funct. Mater.* **2014**, *24*, 7373.

[30] H. Yuan, X. Liu, F. Afshinmanesh, W. Li, G. Xu, J. Sun, B. Lian, A. G. Curto, G. Ye, Y. Hikita, Z. Shen, S.-C. Zhang, X. Chen, M. Brongersma, H. Y. Hwang, Y. Cui, *Nat. Nanotechnol.* **2015**, *10*, 707.

[31] K. K. Manga, J. Wang, M. Lin, J. Zhang, M. Nesladek, V. Nalla, W. Ji, K. P. Loh, *Adv. Mater.* **2012**, *24*, 1697.

[32] H. Wang, Q. Chen, L. Wen, S. Song, X. Hu, G. Xu, *Photonics Res.* **2015**, *3*, 329.

[33] W.-X. Zhou, Y. Shen, E.-T. Hu, Y. Zhao, M.-Y. Sheng, Y.-X. Zheng, S.-Y. Wang, Y.-P. Lee, C.-Z. Wang, D. W. Lynch, L.-Y. Chen, *Opt. Express* **2012**, *20*, 28953.

[34] J. Yan, M. H. Kim, J. A. Elle, A. B. Sushkov, G. S. Jenkins, H. M. Milchberg, M. S. Fuhrer, H. D. Drew, *Nat. Nanotechnol.* **2012**, *7*, 472.

[35] Z. Li, S. Butun, K. Aydin, *ACS Photonics* **2015**, *2*, 183.

[36] Y.-T. Yoon, S.-S. Lee, *Opt. Express* **2010**, *18*, 5344.

[37] J. Guo, C. M. Huard, Y. Yang, Y. J. Shin, K.-T. Lee, L. J. Guo, *Adv. Opt. Mater.* **2014**, *2*, 435.

[38] K.-T. Lee, M. Fukuda, S. Joglekar, L. J. Guo, *J. Mater. Chem. C* **2015**, *3*, 5377.

[39] J. H. Han, D.-Y. Kim, D. Kim, K. C. Choi, *Sci. Rep.* **2016**, *6*, 29341.

[40] Z. Yang, Y. Zhou, Y. Chen, Y. Wang, P. Dai, Z. Zhang, H. Duan, *Adv. Opt. Mater.* **2016**, *4*, 1196.

[41] S. S. Mirshafieyan, H. Guo, J. Guo, *IEEE Photonics J.* **2016**, *8*, 1.

[42] G. Yoo, S. L. Choi, S. J. Park, K.-T. Lee, S. Lee, M. S. Oh, J. Heo, H. J. Park, *Sci. Rep.* **2017**, *7*, 40945.

[43] K. Mao, W. Shen, C. Yang, X. Fang, W. Yuan, Y. Zhang, X. Liu, *Sci. Rep.* **2016**, *6*, 19289.

[44] C. Yang, K. Mao, W. Shen, B. Fang, X. Fang, X. Zhang, Y. Zhang, X. Liu, *Appl. Phys. Lett.* **2016**, *109*, 241104.

[45] C. Genet, T. W. Ebbesen, *Nature* **2007**, *445*, 39.

[46] K.-T. Lee, C. Ji, D. Banerjee, L. J. Guo, *Laser Photonics Rev.* **2015**, *9*, 354.

[47] V. R. Shrestha, S.-S. Lee, E.-S. Kim, D.-Y. Choi, *Sci. Rep.* **2014**, *4*, 4921.

[48] W. Yue, S.-S. Lee, E.-S. Kim, *Opt. Express* **2016**, *24*, 17115.

[49] P. Ji, C.-S. Park, S. Gao, S.-S. Lee, D.-Y. Choi, *Opt. Express* **2017**, *25*, 2153.

[50] M. A. Kats, R. Blanchard, P. Genevet, F. Capasso, *Nat. Mater.* **2013**, *12*, 20.

[51] K.-T. Lee, S. Seo, J. Y. Lee, L. J. Guo, *Adv. Mater.* **2014**, *26*, 6324.

[52] M. A. Kats, F. Capasso, *Laser Photonics Rev.* **2016**, *10*, 735.

[53] K.-T. Lee, S. Seo, J. Y. Lee, L. J. Guo, *Appl. Phys. Lett.* **2014**, *104*, 231112.

[54] K.-T. Lee, J.-Y. Jang, S. J. Park, U. K. Thakur, C. Ji, L. J. Guo, H. J. Park, *Optica* **2016**, *3*, 1489.

[55] C.-S. Park, V. R. Shrestha, S.-S. Lee, E.-S. Kim, D.-Y. Choi, *Sci. Rep.* **2015**, *5*, 8467.

[56] C.-S. Park, V. R. Shrestha, S.-S. Lee, D.-Y. Choi, *Sci. Rep.* **2016**, *6*, 25496.

[57] Y.-K. R. Wu, A. E. Hollowell, C. Zhang, L. J. Guo, *Sci. Rep.* **2013**, *3*, 1194.

[58] C. Yang, W. Shen, Y. Zhang, H. Peng, X. Zhang, X. Liu, *Opt. Express* **2014**, *22*, 11384.

[59] M. Born, E. Wolf, *Principles of Optics,* 7th Ed., Cambridge University Press, New York, NY, USA **1999**.

[60] K.-T. Lee, J. Y. Lee, S. Seo, L. J. Guo, *Light: Sci. Appl.* **2014**, *3*, e215.

[61] J. Y. Lee, K.-T. Lee, S. Seo, L. J. Guo, *Sci. Rep.* **2014**, *4*, 4192.

[62] K.-T. Lee, J. Y. Lee, S. Seo, L. J. Guo, *IEEE J. Photovoltaics* **2015**, *5*, 1654.

[63] K.-T. Lee, J. Y. Lee, T. Xu, H. J. Park, L. J. Guo, *J. Opt.* **2016**, *18*, 064003.

[64] K.-T. Lee, L. J. Guo, J. H. Park, *Molecules* **2016**, *21*, 475.

[65] B. Y. Zheng, Y. Wang, P. Nordlander, N. J. Halas, *Adv. Mater.* **2014**, *26*, 6318.

[66] H. J. Park, T. Xu, J. Y. Lee, A. Ledbetter, L. J. Guo, *ACS Nano* **2011**, *5*, 7055.

[67] W. Zhang, M. Anaya, G. Lozano, M. E. Calvo, M. B. Johnston, H. Míguez, H. J. Snaith, *Nano. Lett.* **2015**, *15*, 1698.

[68] M. Fukuda, K.-T. Lee, J. Y. Lee, L. J. Guo, *IEEE J. Photovoltaics* **2014**, *4*, 1337.

[69] Y.-H. Chen, C.-W. Chen, Z.-Y. Huang, W.-C. Lin, L.-Y. Lin, F. Lin, K.-T. Wong, H.-W. Lin, *Adv. Mater.* **2014**, *26*, 1129.

[70] J.-H. Lu, Y.-L. Yu, S.-R. Chuang, C.-H. Yeh, C.-P. Chen, *J. Phys. Chem. C* **2016**, *120*, 4233.

[71] K.-T. Lee, S. Seo, L. J. Guo, *Adv. Opt. Mater.* **2015**, *3*, 347.

[72] K.-T. Lee, J.-Y. Jang, S. J. Park, C. Ji, S.-M. Yang, L. J. Guo, H. J. Park, *Adv. Opt. Mater.* **2016**, *4*, 1696.

[73] S. S. Wang, R. Magnusson, *Appl. Opt.* **1993**, *32*, 2606.

[74] S. Tibuleac, R. Magnusson, *J. Opt. Soc. Am. A* **1997**, *14*, 1617.

[75] Z. S. Liu, S. Tibuleac, D. Shin, P. P. Young, R. Magnusson, *Opt. Lett.* **1998**, *23*, 1556.

[76] C.-T. Wang, H.-H. Hou, P.-C. Chang, C.-C. Li, H.-C. Jau, Y. Hung, Jr., T.-H. Lin, *Opt. Express* **2016**, *24*, 22892.

[77] M. J. Uddin, R. Magnusson, *Opt. Express* **2013**, *21*, 12495.

[78] M. J. Uddin, T. Khaleque, R. Magnusson, *Opt. Express* **2014**, *22*, 12307.

[79] I. Koirala, V. R. Shrestha, C.-S. Park, S.-S. Lee, D.-Y. Choi, *Sci. Rep.* **2017**, *7*, 40073.

[80] Y.-T. Yoon, H.-S. Lee, S.-S. Lee, S. H. Kim, J.-D. Park, K.-D. Lee, *Opt. Express* **2008**, *16*, 2374.

[81] C.-H. Park, Y.-T. Yoon, S.-S. Lee, *Opt. Express* **2012**, *20*, 23769.

[82] A. F. Kaplan, T. Xu, L. J. Guo, *Appl. Phys. Lett.* **2011**, *99*, 143111.

[83] V. R. Shrestha, S.-S. Lee, E.-S. Kim, D.-Y. Choi, *Sci. Rep.* **2015**, *5*, 12450.

[84] E.-H. Cho, H.-S. Kim, B.-H. Cheong, P. Oleg, W. Xianyua, J.-S. Sohn, D.-J. Ma, H.-Y. Choi, N.-C. Park, Y.-P. Park, *Opt. Express* **2009**, *17*, 8621.

[85] E.-H. Cho, H.-S. Kim, J.-S. Sohn, C.-Y. Moon, N.-C. Park, Y.-P. Park, *Opt. Express* **2010**, *18*, 27712.

[86] H. Kim, J. Ge, J. Kim, S.-e. Choi, H. Lee, H. Lee, W. Park, Y. Yin, S. Kwon, *Nat. Photonics* **2009**, *3*, 534.

[87] H. Nam, K. Song, D. Ha, T. Kim, *Sci. Rep.* **2016**, *6*, 30885.

[88] S. Y. Lee, S.-H. Kim, H. Hwang, J. Y. Sim, S.-M. Yang, *Adv. Mater.* **2014**, *26*, 2391.

[89] H. S. Lee, J. H. Kim, J.-S. Lee, J. Y. Sim, J. Y. Seo, Y.-K. Oh, S.-M. Yang, S.-H. Kim, *Adv. Mater.* **2014**, *26*, 5801.

[90] S. Y. Lee, J. Choi, J.-R. Jeong, J. H. Shin, S.-H. Kim, *Adv. Mater.* **2017**, *29*, 1605450.

[91] O. Berger, E. Yoskovitz, L. Adler-Abramovich, E. Gazit, *Adv. Mater.* **2016**, *28*, 2195.

[92] D. Gur, B. Leshem, V. Farstey, D. Oron, L. Addadi, S. Weiner, *Adv. Funct. Mater.* **2016**, *26*, 1393.

[93] A. Sato, N. Iwai, M. Sato, *J. Opt. Soc. Am. A* **2010**, *27*, 1671.

[94] Y. Ye, R. Shao, Y. Zhou, L. Chen, *Appl. Opt.* **2012**, *51*, 5785.

[95] X. Buet, E. Daran, D. Belharet, F. Lozes-Dupuy, A. Monmayrant, O. Gauthier-Lafaye, *Opt. Express* **2012**, *20*, 9322.

[96] A. Sentenac, A.-L. Fehrembach, *J. Opt. Soc. Am. A* **2005**, *22*, 475.

[97] T. Xu, Y.-K. Wu, X. Luo, L. J. Guo, *Nat. Commun.* **2010**, *1*, 59.

[98] D. Inoue, A. Miura, T. Nomura, H. Fujikawa, K. Sato, N. Ikeda, D. Tsuya, Y. Sugimoto, Y. Koide, *Appl. Phys. Lett.* **2011**, *98*, 093113.

[99] M. A. Vincenti, M. Grande, D. de Ceglia, T. Stomeo, V. Petruzzelli, M. De Vittorio, M. Scalora, A. D'Orazio, *Appl. Phys. Lett.* **2012**, *100*, 201107.

[100] S. Yokogawa, S. P. Burgos, H. A. Atwater, *Nano. Lett.* **2012**, *12*, 4349.

[101] K. Kumar, H. Duan, R. S. Hegde, S. C. W. Koh, J. N. Wei, J. K. W. Yang, *Nat. Nanotechnol.* **2012**, *7*, 557.

[102] J. S. Clausen, E. Højlund-Nielsen, A. B. Christiansen, S. Yazdi, M. Grajower, H. Taha, U. Levy, A. Kristensen, N. A. Mortensen, *Nano. Lett.* **2014**, *14*, 4499.

[103] B. Zeng, Y. Gao, F. J. Bartoli, *Sci. Rep.* **2013**, *3*, 2840.

[104] H. Yun, S.-Y. Lee, K. Hong, J. Yeom, B. Lee, *Nat. Commun.* **2015**, *6*, 7133.

[105] J. Wang, Q. Fan, S. Zhang, Z. Zhang, H. Zhang, Y. Liang, X. Cao, T. Xu, *Appl. Phys. Lett.* **2017**, *110*, 031110.

[106] Y. S. Do, J. H. Park, B. Y. Hwang, S.-M. Lee, B.-K. Ju, K. C. Choi, *Adv. Opt. Mater.* **2013**, *1*, 133.

[107] D. Franklin, Y. Chen, A. Vazquez-Guardado, S. Modak, J. Boroumand, D. Xu, S.-T. Wu, D. Chanda, *Nat. Commun.* **2015**, *6*, 7337.

[108] M. Miyata, H. Hatada, J. Takahara, *Nano. Lett.* **2016**, *16*, 3166.

[109] J. Olson, A. Manjavacas, T. Basu, D. Huang, A. E. Schlather, B. Zheng, N. J. Halas, P. Nordlander, S. Link, *ACS Nano* **2016**, *10*, 1108.

[110] S. J. Tan, L. Zhang, D. Zhu, X. M. Goh, Y. M. Wang, K. Kumar, C.-W. Qiu, J. K. W. Yang, *Nano. Lett.* **2014**, *14*, 4023.

[111] T. Chen, B. M. Reinhard, *Adv. Mater.* **2016**, *28*, 3522.

[112] F. Cheng, J. Gao, T. S. Luk, X. Yang, *Sci. Rep.* **2015**, *5*, 11045.

[113] F. Cheng, J. Gao, L. Stan, D. Rosenmann, D. Czaplewski, X. Yang, *Opt. Express* **2015**, *23*, 14552.

[114] G. Si, Y. Zhao, J. Lv, M. Lu, F. Wang, H. Liu, N. Xiang, T. J. Huang, A. J. Danner, J. Teng, Y. J. Liu, *Nanoscale* **2013**, *5*, 6243.

[115] V. R. Shrestha, S.-S. Lee, E.-S. Kim, D.-Y. Choi, *Nano. Lett.* **2014**, *14*, 6672.

[116] L. Duempelmann, D. Casari, A. Luu-Dinh, B. Gallinet, L. Novotny, *ACS Nano* **2015**, *9*, 12383.

[117] K. Saito, T. Tatsuma, *Adv. Opt. Mater.* **2015**, *3*, 883.

[118] K. Xiong, G. Emilsson, A. Maziz, X. Yang, L. Shao, E. W. H. Jager, A. B. Dahlin, *Adv. Mater.* **2016**, *28*, 9956.

[119] C. Yang, W. Shen, J. Zhou, X. Fang, D. Zhao, X. Zhang, C. Ji, B. Fang, Y. Zhang, X. Liu, L. J. Guo, *Adv. Opt. Mater.* **2016**, *4*, 1981.

[120] T. D. James, P. Mulvaney, A. Roberts, *Nano Lett.* **2016**, *16*, 3817.

[121] Z. Yang, Y. Chen, Y. Zhou, Y. Wang, P. Dai, X. Zhu, H. Duan, *Adv. Opt. Mater.* **2017**, *5*, 1700029.

[122] X. Duan, S. Kamin, N. Liu, *Nat. Commun.* **2017**, *8*, 14606.

[123] T. W. Ebbesen, H. J. Lezec, H. F. Ghaemi, T. Thio, P. A. Wolff, *Nature* **1998**, *391*, 667.

[124] A. Wang, P. Gill, A. Molnar, *Appl. Opt.* **2009**, *48*, 5897.

[125] L. Shi, P. Pottier, Y.-A. Peter, M. Skorobogatiy, *Opt. Express* **2008**, *16*, 17962.

[126] E. D. Kosten, J. H. Atwater, J. Parsons, A. Polman, H. A. Atwater, *Light: Sci. Appl.* **2013**, *2*, e45.

[127] A. P. Raman, M. A. Anoma, L. Zhu, E. Rephaeli, S. Fan, *Nature* **2014**, *515*, 540.

[128] X. Zhu, C. Vannahme, E. Højlund-Nielsen, N. A. Mortensen, A. Kristensen, *Nat. Nanotechnol.* **2016**, *11*, 325.

[129] A. Kristensen, J. K. W. Yang, S. I. Bozhevolnyi, S. Link, P. Nordlander, N. J. Halas, N. A. Mortensen, *Nat. Rev. Mater.* **2016**, *2*, 16088.

[130] L. Wang, R. J. H. Ng, S. Safari Dinachali, M. Jalali, Y. Yu, J. K. W. Yang, *ACS Photonics* **2016**, *3*, 627.

[131] R. Yu, P. Mazumder, N. F. Borrelli, A. Carrilero, D. S. Ghosh, R. A. Maniyara, D. Baker, F. J. García de Abajo, V. Pruneri, *ACS Photonics* **2016**, *3*, 1194.

[132] H. Cheng, S. Shu, Z. Lu, C. Lee, S. Zeng, J. Lu, Y. Y. Li, *J. Appl. Phys.* **2014**, *116*, 153511.

[133] A. Moreau, C. Ciraci, J. J. Mock, R. T. Hill, Q. Wang, B. J. Wiley, A. Chilkoti, D. R. Smith, *Nature* **2012**, *492*, 86.

[134] X. Liu, T. Starr, A. F. Starr, W. J. Padilla, *Phys. Rev. Lett.* **2010**, *104*, 207403.

[135] T. Maier, H. Brueckl, *Opt. Lett.* **2010**, *35*, 3766.

[136] T. Maier, H. Brückl, *Opt. Lett.* **2009**, *34*, 3012.

[137] H. Tao, E. A. Kadlec, A. C. Strikwerda, K. Fan, W. J. Padilla, R. D. Averitt, E. A. Shaner, X. Zhang, *Opt. Express* **2011**, *19*, 21620.

[138] W. W. Salisbury, *US 2599944*, **1952**.

[139] S. Shu, Z. Li, Y. Y. Li, *Opt. Express* **2013**, *21*, 25307.

[140] H. Shin, M. F. Yanik, S. Fan, R. Zia, M. L. Brongersma, *Appl. Phys. Lett.* **2004**, *84*, 4421.

[141] M. Yan, *J. Opt.* **2013**, *15*, 025006.

[142] K. M. Hedayati, F. Faupel, M. Elbahri, *Materials* **2014**, *7*, 1221.

[143] C. M. Watts, X. Liu, W. J. Padilla, *Adv. Mater.* **2012**, *24*, OP98.

[144] Y. Cui, Y. He, Y. Jin, F. Ding, L. Yang, Y. Ye, S. Zhong, Y. Lin, S. He, *Laser Photonics Rev.* **2014**, *8*, 495.

[145] J. Le Perchec, P. Quémerais, A. Barbara, T. López-Ríos, *Phys. Rev. Lett.* **2008**, *100*, 066408.

[146] T. López-Rios, D. Mendoza, F. J. García-Vidal, J. Sánchez-Dehesa, B. Pannetier, *Phys. Rev. Lett.* **1998**, *81*, 665.

[147] N. Liu, M. Mesch, T. Weiss, M. Hentschel, H. Giessen, *Nano Lett.* **2010**, *10*, 2342.

[148] A. Cattoni, P. Ghenuche, A.-M. Haghiri-Gosnet, D. Decanini, J. Chen, J.-L. Pelouard, S. Collin, *Nano Lett.* **2011**, *11*, 3557.

[149] N. I. Landy, S. Sajuyigbe, J. J. Mock, D. R. Smith, W. J. Padilla, *Phys. Rev. Lett.* **2008**, *100*, 207402.

[150] A. V. Kabashin, P. Evans, S. Pastkovsky, W. Hendren, G. A. Wurtz, R. Atkinson, R. Pollard, V. A. Podolskiy, A. V. Zayats, *Nat. Mater.* **2009**, *8*, 867.

[151] Y. He, H. Deng, X. Jiao, S. He, J. Gao, X. Yang, *Opt. Lett.* **2013**, *38*, 1179.

[152] Z. Li, E. Palacios, S. Butun, H. Kocer, K. Aydin, *Sci. Rep.* **2015**, *5*, 15137.

[153] F. Ding, J. Dai, Y. Chen, J. Zhu, Y. Jin, S. I. Bozhevolnyi, *Sci. Rep.* **2016**, *6*, 39445.

[154] W. Wang, Y. Qu, K. Du, S. Bai, J. Tian, M. Pan, H. Ye, M. Qiu, Q. Li, *Appl. Phys. Lett.* **2017**, *110*, 101101.

[155] K. Aydin, V. E. Ferry, R. M. Briggs, H. A. Atwater, *Nat. Commun.* **2011**, *2*, 517.

[156] S. Butun, K. Aydin, *Opt. Express* **2014**, *22*, 19457.

[157] I. Khan, H. Keshmiri, F. Kolb, T. Dimopoulos, E. J. W. List-Kratochvil, J. Dostalek, *Adv. Opt. Mater.* **2016**, *4*, 435.

[158] J. Cong, Z. Zhou, B. Yun, L. Lv, H. Yao, Y. Fu, N. Ren, *Opt. Lett.* **2016**, *41*, 1965.

[159] G. Kajtár, M. Kafesaki, E. N. Economou, C. M. Soukoulis, *J. Phys. D: Appl. Phys.* **2016**, *49*, 055104.

[160] Y.-F. Huang, S. Chattopadhyay, Y.-J. Jen, C.-Y. Peng, T.-A. Liu, Y.-K. Hsu, C.-L. Pan, H.-C. Lo, C.-H. Hsu, Y.-H. Chang, C.-S. Lee, K.-H. Chen, L.-C. Chen, *Nat. Nanotechnol.* **2007**, *2*, 770.

[161] K. Mizuno, J. Ishii, H. Kishida, Y. Hayamizu, S. Yasuda, D. N. Futaba, M. Yumura, K. Hata, *Proc. Natl. Acad. Sci. USA* **2009**, *106*, 6044.

[162] J. Zhu, Z. Yu, G. F. Burkhard, C.-M. Hsu, S. T. Connor, Y. Xu, Q. Wang, M. McGehee, S. Fan, Y. Cui, *Nano Lett.* **2009**, *9*, 279.

[163] F.-D. Lai, W.-Y. Li, *Integr. Ferroelectr.* **2013**, *145*, 158.

[164] F.-D. Lai, W.-Y. Li, K.-C. Chang, Y.-Z. Wang, P.-L. Chi, J.-Y. Su, *Integr. Ferroelectr.* **2012**, *137*, 77.

[165] T. K. Tsai, S. J. Hsueh, J. S. Fang, *J. Electron. Mater.* **2014**, *43*, 229.

[166] Z. Y. Nuru, M. Msimanga, T. F. G. Muller, C. J. Arendse, C. Mtshali, M. Maaza, *Sol. Energy* **2015**, *111*, 357.

[167] M.-H. Liu, E.-T. Hu, Y. Yao, K.-Y. Zang, N. He, J. Li, Y.-X. Zheng, S.-Y. Wang, O. Yoshie, Y. Lee, C.-Z. Wang, D. W. Lynch, L.-Y. Chen, *Opt. Express* **2014**, *22*, A1843.

[168] H. Deng, Z. Li, L. Stan, D. Rosenmann, D. Czaplewski, J. Gao, X. Yang, *Opt. Lett.* **2015**, *40*, 2592.

[169] H. Wang, L. Wang, *Opt. Express* **2013**, *21*, A1078.

[170] K. Gorgulu, A. Gok, M. Yilmaz, K. Topalli, N. Bıyıklı, A. K. Okyay, *Sci. Rep.* **2016**, *6*, 38589.

[171] W. Wang, S. Wu, K. Reinhardt, Y. Lu, S. Chen, *Nano Lett.* **2010**, *10*, 2012.

[172] W. Li, U. Guler, N. Kinsey, G. V. Naik, A. Boltasseva, J. Guan, V. M. Shalaev, A. V. Kildishev, *Adv. Mater.* **2014**, *26*, 7959.

[173] U. Guler, A. Boltasseva, V. M. Shalaev, *Science* **2014**, *344*, 263.

[174] P. Nagpal, S. E. Han, A. Stein, D. J. Norris, *Nano Lett.* **2008**, *8*, 3238.

[175] K.-T. Lee, C. Ji, L. J. Guo, *Appl. Phys. Lett.* **2016**, *108*, 031107.

[176] C. Yang, C. Ji, W. Shen, K.-T. Lee, Y. Zhang, X. Liu, L. J. Guo, *ACS Photonics* **2016**, *3*, 590.

[177] Y. Q. Ye, Y. Jin, S. He, *J. Opt. Soc. Am. B* **2010**, *27*, 498.

[178] T. Jang, H. Youn, Y. J. Shin, L. J. Guo, *ACS Photonics* **2014**, *1*, 279.

[179] Y. Cui, J. Xu, K. H. Fung, Y. Jin, A. Kumar, S. He, N. X. Fang, *Appl. Phys. Lett.* **2011**, *99*, 253101.

[180] Y. Cui, K. H. Fung, J. Xu, H. Ma, Y. Jin, S. He, N. X. Fang, *Nano Lett.* **2012**, *12*, 1443.

[181] D. Ji, H. Song, X. Zeng, H. Hu, K. Liu, N. Zhang, Q. Gan, *Sci. Rep.* **2014**, *4*, 4498.

[182] J. Zhou, A. F. Kaplan, L. Chen, L. J. Guo, *ACS Photonics* **2014**, *1*, 618.

[183] M. K. Hedayati, M. Javaherirahim, B. Mozooni, R. Abdelaziz, A. Tavassolizadeh, V. S. K. Chakravadhanula, V. Zaporojtchenko, T. Strunkus, F. Faupel, M. Elbahri, *Adv. Mater.* **2011**, *23*, 5410.

[184] Y. Ebihara, R. Ota, T. Noriki, M. Shimojo, K. Kajikawa, *Sci. Rep.* **2015**, *5*, 15992.

[185] M. K. Hedayati, F. Faupel, M. Elbahri, *Appl. Phys. A* **2012**, *109*, 769.

[186] M. K. Hedayati, A. U. Zillohu, T. Strunkus, F. Faupel, M. Elbahri, *Appl. Phys. Lett.* **2014**, *104*, 041103.

[187] L. Zhou, Y. Tan, J. Wang, W. Xu, Y. Yuan, W. Cai, S. Zhu, J. Zhu, *Nat. Photonics* **2016**, *10*, 393.

[188] B. J. Lee, Y.-B. Chen, S. Han, F.-C. Chiu, H. J. Lee, *J. Heat Transfer* **2014**, *136*, 072702.

[189] X. Jia, X. Wang, C. Yuan, Q. Meng, Z. Zhou, *J. Appl. Phys.* **2016**, *120*, 033101.

[190] P. Zhu, L. J. Guo, *Appl. Phys. Lett.* **2012**, *101*, 241116.

[191] C. T. Riley, J. S. T. Smalley, J. R. J. Brodie, Y. Fainman, D. J. Sirbuly, Z. Liu, *Proc. Natl. Acad. Sci. USA* **2017**, *114*, 1264.

[192] Z. Liu, H. Lee, Y. Xiong, C. Sun, X. Zhang, *Science* **2007**, *315*, 1686.

[193] D. Schurig, J. J. Mock, B. J. Justice, S. A. Cummer, J. B. Pendry, A. F. Starr, D. R. Smith, *Science* **2006**, *314*, 977.

[194] X. Zhang, Z. Liu, *Nat. Mater.* **2008**, *7*, 435.

[195] H. Shi, J. G. Ok, H. W. Baac, L. J. Guo, *Appl. Phys. Lett.* **2011**, *99*, 211103.

[196] Z.-P. Yang, L. Ci, J. A. Bur, S.-Y. Lin, P. M. Ajayan, *Nano Lett.* **2008**, *8*, 446.

[197] F. J. García-Vidal, J. M. Pitarke, J. B. Pendry, *Phys. Rev. Lett.* **1997**, *78*, 4289.

[198] E. Reyes, A. A. Krokhin, J. Roberts, *Phys. Rev. B* **2005**, *72*, 155118.

[199] T. de los Arcos, P. Oelhafen, D. Mathys, *Nanotechnology* **2007**, *18*, 265706.

[200] E. Rephaeli, S. Fan, *Appl. Phys. Lett.* **2008**, *92*, 211107.

[201] S. Chhajed, M. F. Schubert, J. K. Kim, E. F. Schubert, *Appl. Phys. Lett.* **2008**, *93*, 251108.

[202] T.-H. Her, R. J. Finlay, C. Wu, S. Deliwala, E. Mazur, *Appl. Phys. Lett.* **1998**, *73*, 1673.

[203] J. Zhou, M. Hildebrandt, M. Lu, *J. Appl. Phys.* **2011**, *109*, 053513.

[204] R. Torres, V. Vervisch, M. Halbwax, T. Sarnet, P. Delaporte, M. Sentis, J. Ferreira, D. Barakel, S. Bastide, F. Torregrosa, E. H., *J. Optoelectron. Adv. Mater.* **2010**, *12*, 621.

[205] Y. Qiu, H.-C. Hao, J. Zhou, M. Lu, *Opt. Express* **2012**, *20*, 22087.

[206] A. Rahman, A. Ashraf, H. Xin, X. Tong, P. Sutter, M. D. Eisaman, C. T. Black, *Nat. Commun.* **2015**, *6*, 5963.

[207] J. Zhou, X. Chen, L. J. Guo, *Adv. Mater.* **2016**, *28*, 3017.

[208] H. N. S. Krishnamoorthy, Z. Jacob, E. Narimanov, I. Kretzschmar, V. M. Menon, *Science* **2012**, *336*, 205.

[209] C. L. Cortes, W. Newman, S. Molesky, Z. Jacob, *J. Opt.* **2012**, *14*, 063001.

[210] Y. Guo, C. L. Cortes, S. Molesky, Z. Jacob, *Appl. Phys. Lett.* **2012**, *101*, 131106.

[211] Y. Guo, Z. Jacob, *Opt. Express* **2013**, *21*, 15014.

[212] K.-T. Lee, S. Y. Han, H. J. Park, *Adv. Opt. Mater.* **2017**, 1700284.

[213] C. Zhang, D. Zhao, D. Gu, H. Kim, T. Ling, Y.-K. R. Wu, L. J. Guo, *Adv. Mater.* **2014**, *26*, 5696.

[214] D. Gu, C. Zhang, Y.-K. Wu, L. J. Guo, *ACS Nano* **2014**, *8*, 10343.

[215] C. Zhang, N. Kinsey, L. Chen, C. Ji, M. Xu, M. Ferrera, X. Pan, V. M. Shalaev, A. Boltasseva, L. J. Guo, *Adv. Mater.* **2017**, *29*, 1605177.

[216] A. Sobhani, A. Manjavacas, Y. Cao, M. J. McClain, F. J. García de Abajo, P. Nordlander, N. J. Halas, *Nano Lett.* **2015**, *15*, 6946.

[217] B. Luk'yanchuk, N. I. Zheludev, S. A. Maier, N. J. Halas, P. Nordlander, H. Giessen, C. T. Chong, *Nat. Mater.* **2010**, *9*, 707.

[218] D. Liu, H. Yu, Z. Yang, Y. Duan, *Nano Res.* **2016**, *9*, 2354.

[219] D. Liu, D. M. Bierman, A. Lenert, H.-T. Yu, Z. Yang, E. N. Wang, Y.-Y. Duan, *Opt. Express* **2015**, *23*, A1491.

[220] D. Liu, Q. Li, *Nano Energy* **2017**, *34*, 172.

[221] M. Jafari, L. J. Guo, M. Rais-Zadeh, *Proc. SPIE* **2017**, *10100*, 101000I.

[222] H. Dotan, O. Kfir, E. Sharlin, O. Blank, M. Gross, I. Dumchin, G. Ankonina, A. Rothschild, *Nat. Mater.* **2013**, *12*, 158.

[223] J. Park, J.-H. Kang, A. P. Vasudev, D. T. Schoen, H. Kim, E. Hasman, M. L. Brongersma, *ACS Photonics* **2014**, *1*, 812.

[224] Q. Xie, M. H. Hong, H. L. Tan, G. X. Chen, L. P. Shi, T. C. Chong, *J. Alloys Compd.* **2008**, *449*, 261.

[225] F. Yu, P. Li, H. Shen, S. Mathur, C.-M. Lehr, U. Bakowsky, F. Mücklich, *Biomaterials* **2005**, *26*, 2307.

[226] S. H. Ahn, L. J. Guo, *Adv. Mater.* **2008**, *20*, 2044.

[227] S. H. Ahn, L. J. Guo, *ACS Nano* **2009**, *3*, 2304.

[228] B. M. Boyle, T. A. French, R. M. Pearson, B. G. McCarthy, G. M. Miyake, *ACS Nano* **2017**, *11*, 3052.

[229] W. Wu, D. Dey, O. G. Memis, A. Katsnelson, H. Mohseni, *Nanoscale Res. Lett.* **2008**, *3*, 351.

[230] C. L. Haynes, R. P. Van Duyne, *J. Phys. Chem. B* **2001**, *105*, 5599.

[231] J. C. Hulteen, R. P. Van Duyne, *J. Vac. Sci. Technol. A* **1995**, *13*, 1553.

[232] H. H. Solak, C. Dais, F. Clube, *Opt. Express* **2011**, *19*, 10686.

[233] S. Xie, B. Schurink, E. J. W. Berenschot, *J. Vac. Sci. Technol. B* **2016**, *34*, 06KI02.

Submitted to ADVANCED OPTICAL MATERIALS

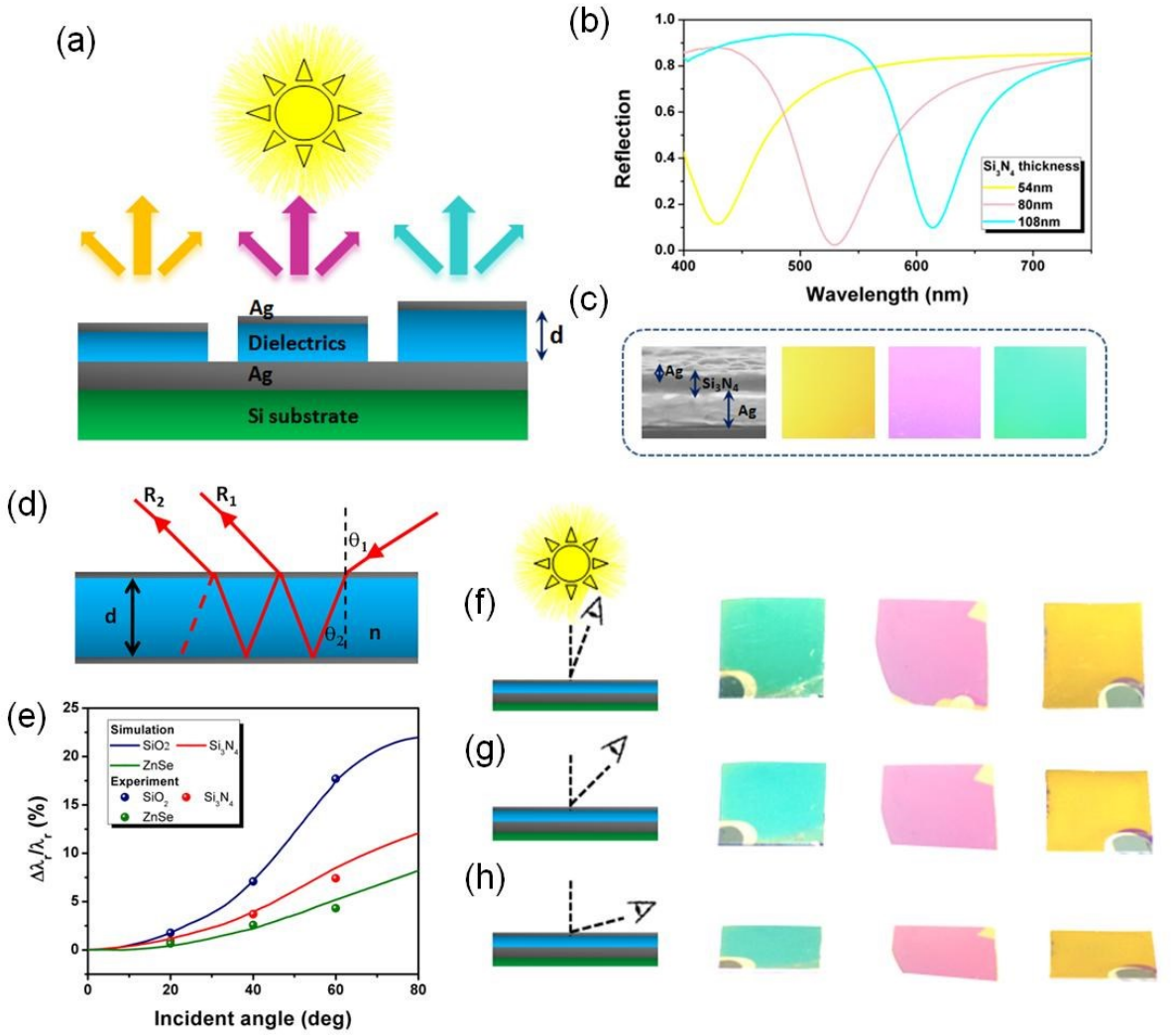

Figure 1. a) Schematic diagram of the proposed reflective F–P color filter. The dielectric cavity length is *d*. The thicknesses of top and bottom metallic layers are fixed as 20 nm and 150 nm, respectively, for different reflective colors. The illumination source is normally incident onto the planar surface with arbitrary polarization. b) Experimentally measured reflection spectra of the cyan, magenta and yellow (CMY) color filters with Si_3N_4 dielectric thicknesses of *d* = 108, 80, and 54 nm. c) SEM and optical images for the CMY colored devices. The device sizes are about 2cm × 2cm. d) Schematic of the F–P etalon structure. The incident and refractive angle is θ_1 and θ_2, respectively. e) Simulation (curve) and experiment (dot) results of devices on the resonant wavelength variation as a function of incident angles. Here the dielectric cavity material of the devices is SiO_2, Si_3N_4, and ZnSe, respectively. f–h) Optical images for the CMY color filters with ZnSe cavity. The images are taken with the reflection angle about f) 20°, g) 45°, and h) 70°.

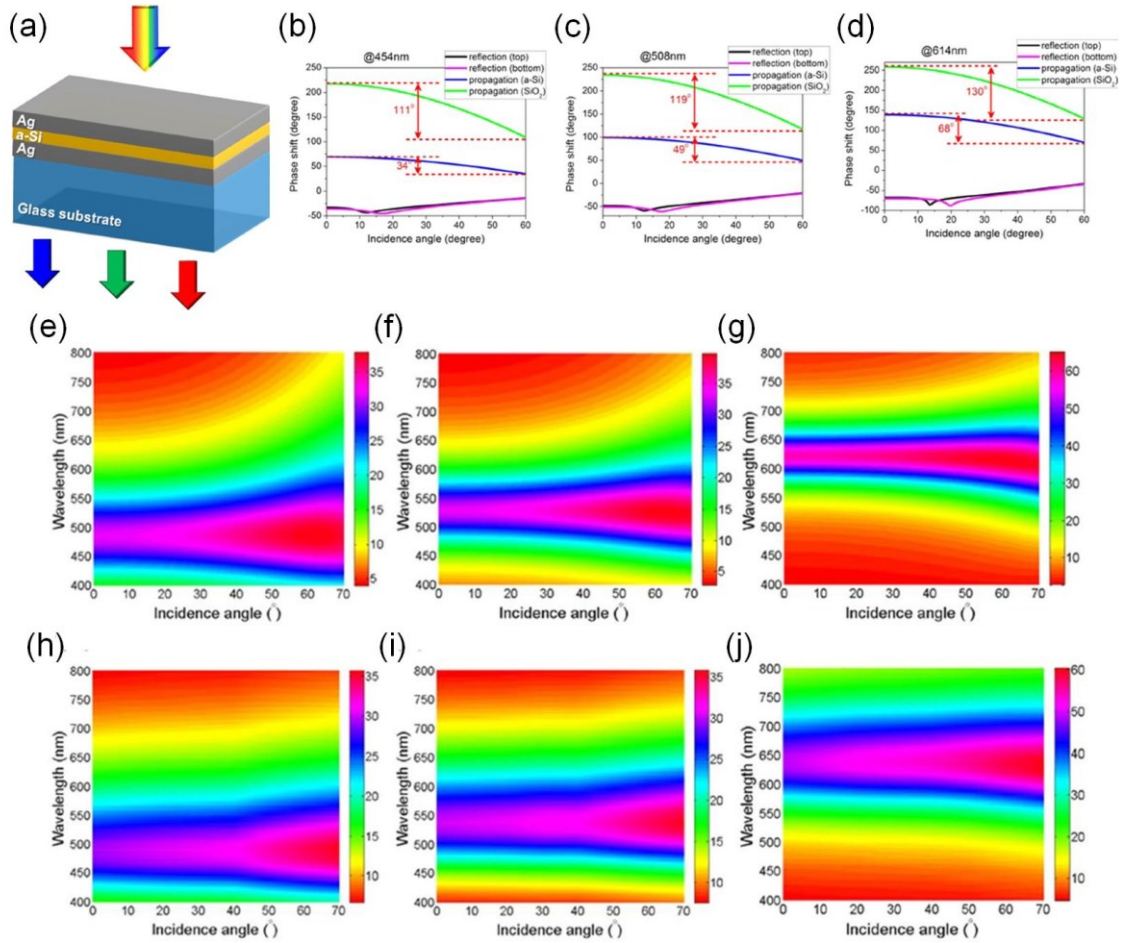

Figure 2. a) A geometry of angle-insensitive color filters comprising a semiconductor layer sandwiched by two thin metal layers on a glass substrate. b–d) Calculated propagation phase accumulation and reflection phase shifts at both the top and bottom a-Si and Ag interfaces as a function of the incident angle for red, green and blue (RGB) transmissive colors. The propagation phase change inside the transparent cavity layer (SiO_2) is also plotted for comparison. E–g) Simulated and h–j) measured angle-resolved transmission spectra of the proposed visible wavelength filters under p-polarized light illumination. The flat dispersion curves indicate that the transmissive resonance wavelengths are retained up to 70° for all three primary colors. Reproduced with permission.[53] Copyright 2014, AIP Publishing LLC.

Submitted to ADVANCED OPTICAL MATERIALS

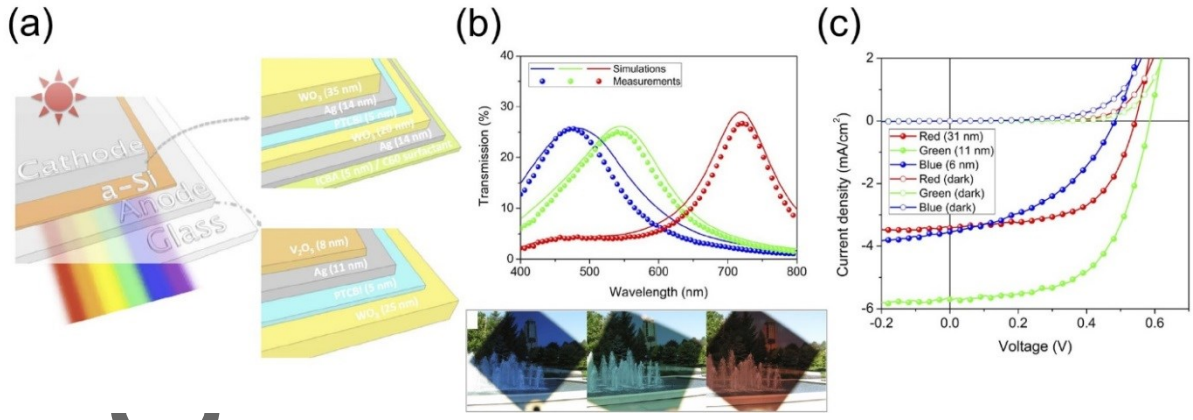

Figure 3. a) A schematic diagram of a colorful, see-through structure that comprises cathode, anode, and ultra-thin undoped a-Si. The cathode is composed of dielectric–metal–dielectric (DMD) and organic layers, and only DMD structure for the anode. The ultra-thin a-Si layer thickness is 31, 11, and 6 nm for the RGB colors, respectively. b) (top) Calculated and measured transmission spectra at normal incidence. (bottom) Photographs of distinct blue, green, and red colors by the fabricated devices. c) Current density-voltage (*J*–*V*) characteristics of the hybrid cells under AM1.5 illumination and dark conditions. Reproduced with permission.[61] Copyright 2014, Nature Publishing Group.

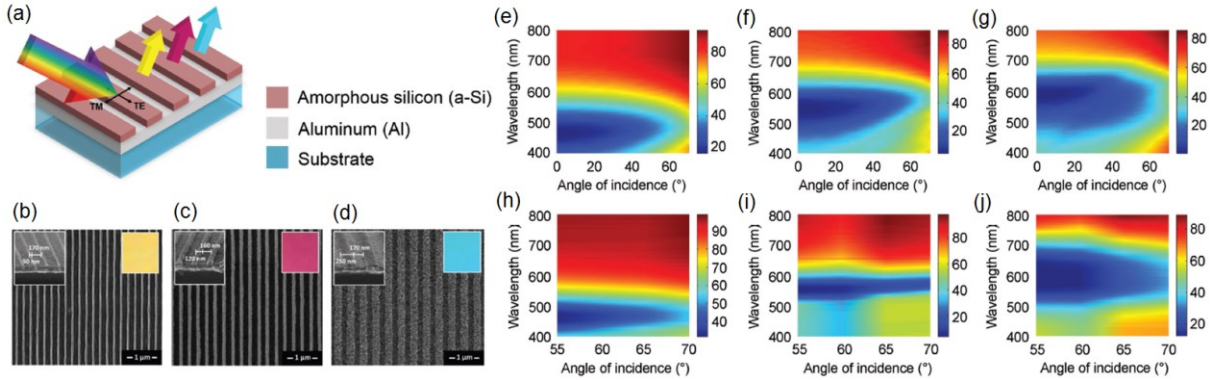

Figure 4. a) Schematic representation of the wide-angle reflective structural color filters consisting of 1D patterned a-Si gratings on an opaque Al bottom layer. Top-view SEM images of fabricated b) Y, c) M, and d) C color filters. Left (right) insets show tilted-angle SEM images (optical images) of the fabricated devices. e–g) Calculated (0°–70°) and h–j) measured (55°–70°) angle-resolved reflection spectra of the reflective structural color filters. Reproduced with permission.[72] Copyright 2016, John Wiley & Sons.

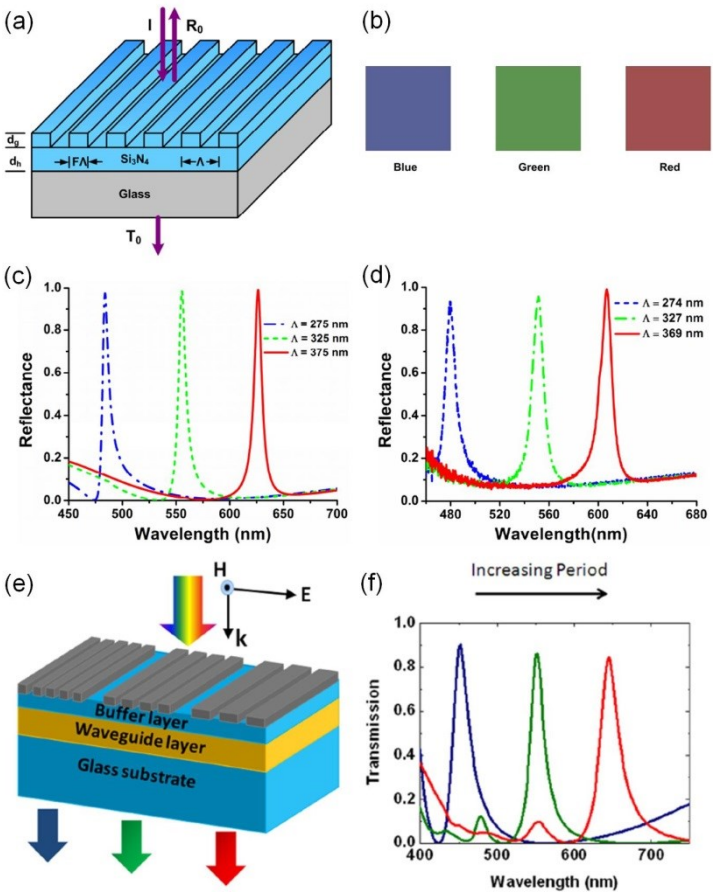

Figure 5. a) Schematic diagram of the GMR-based color filter structures showing the materials and device parameters. d_g = grating depth, d_h = thickness of homogeneous layer, F = fill factor, Λ = period, I = incident light wave, T_0 = zero-order transmittance, and R_0 = zero-order reflectance. b) Perceived colors constructed from the experimentally observed reflectance values. c) Simulated reflectance of the designed color filter array for normally incident s-polarized light that has an electric field vector normal to the plane of incidence and along the grating grooves in (a). d) Measured spectral response of the tunable color filter array. Reproduced with permission.[77] Copyright 2013, Optical Society of America. e) Schematic of the transmissive color filter structure based on metallic GMR effects. f) Simulated transmission spectra of p-polarization incidence (i.e., the electric field is perpendicular to the direction of the subwavelength gratings) when increasing the grating period from 280 to 420 nm, showing that the colors are shifted from blue to red while maintaining the high effciency and high purity. Reproduced with permission.[82] Copyright 2011, AIP Publishing LLC.

Submitted to ADVANCED OPTICAL MATERIALS

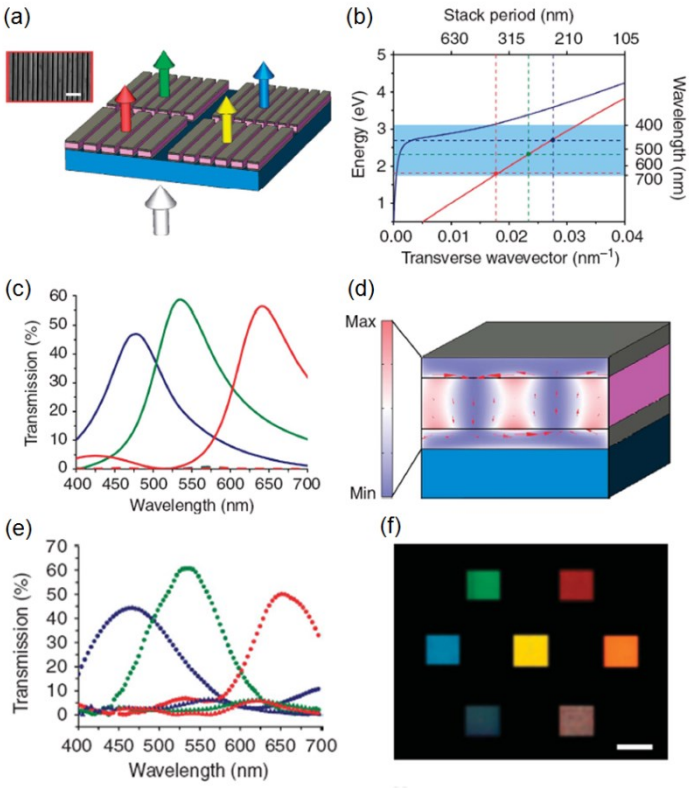

Figure 6. a) Schematic diagram of the plasmonic nanoresonators. The white arrow represents the incident white light and the red, yellow, green and blue arrows represent the transmitted coloured light from the different stack arrays. Grey, pink and blue in the structure indicate the material of aluminium, zinc selenide and magnesium fluoride respectively. Inset is the SEM image of the fabricated device. Scale bar is 1 µm. b) Plasmon dispersions in MIM stack array. Red, green and blue dots correspond to the case of filtering primary RGB colours. Red and blue curves correspond to antisymmetric and symmetric modes respectively. The shaded region indicates the visible range. c) Simulated transmission spectra for the RGB filters. The solid and dash curves correspond to p- and s-polarized light illuminations respectively. d) Cross-section of the time-average magnetic field intensity and electric displacement distribution (red arrow) inside the MDM stack at a wavelength of 650 nm with 360 nm stack period. The colours on the right side represent the constitutive materials, defined as in (a). e) Micrographs of seven plasmonic colour filters illuminated by white light. Scale bar is 10 µm. f) Experimentally measured transmission spectra of three fabricated colour filters corresponding to the RGB colours. The circle and triangle correspond to p- and s-polarized light illuminations respectively. Reproduced with permission.[97] Copyright 2010, Nature Publishing Group.

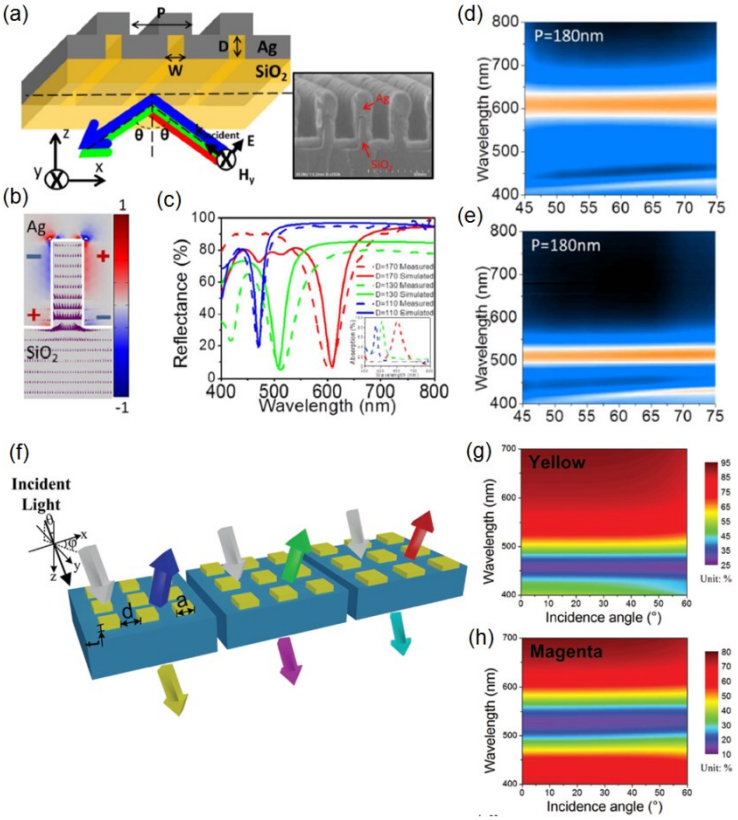

Figure 7. a) A schematic of the metallic nanocavity-based angle-insensitive structural colors and corresponding SEM image of a fabricated device. b) Polarization charge and Poynting vector distribution of light funneled into these nanogrooves, presented with the red–blue surface plot and purple arrows, respectively. c) Reflection (simulated in solid lines and measured in dash lines) and measured absorption spectra (inset, dashed lines) at *D* = 110, 130, and 170 nm in blue, green, and red curves, given fixed *P* = 180 and *W* = 50 nm at normal incidence. d) The angle resolved reflection spectra of this design with sweeping incident illumination angle from 45° to 75° are presented with the following device dimensions d) *P* = 180, *W* = 50, and *D* = 130 nm and e) *P* = 180, *W* = 50, and *D* = 170 nm. Reproduced with permission.[57] Copyright 2013, Nature Publishing Group. f) The schematic geometry of the angle robust reflection/transmission plasmonic filters using localized surface plasmonic resonances in the ultrathin metal patch array structure. g) Simulated transmittance of the transmissive yellow filter of the nanocuboid pattern as a function of wavelength and the angle of incidence for average polarization. h) Simulated transmittance of the transmissive magenta filter of the nanocuboid pattern as a function of wavelength and the angle of incidence for average polarization. Reproduced with permission.[119] Copyright 2016, John Wiley & Sons.

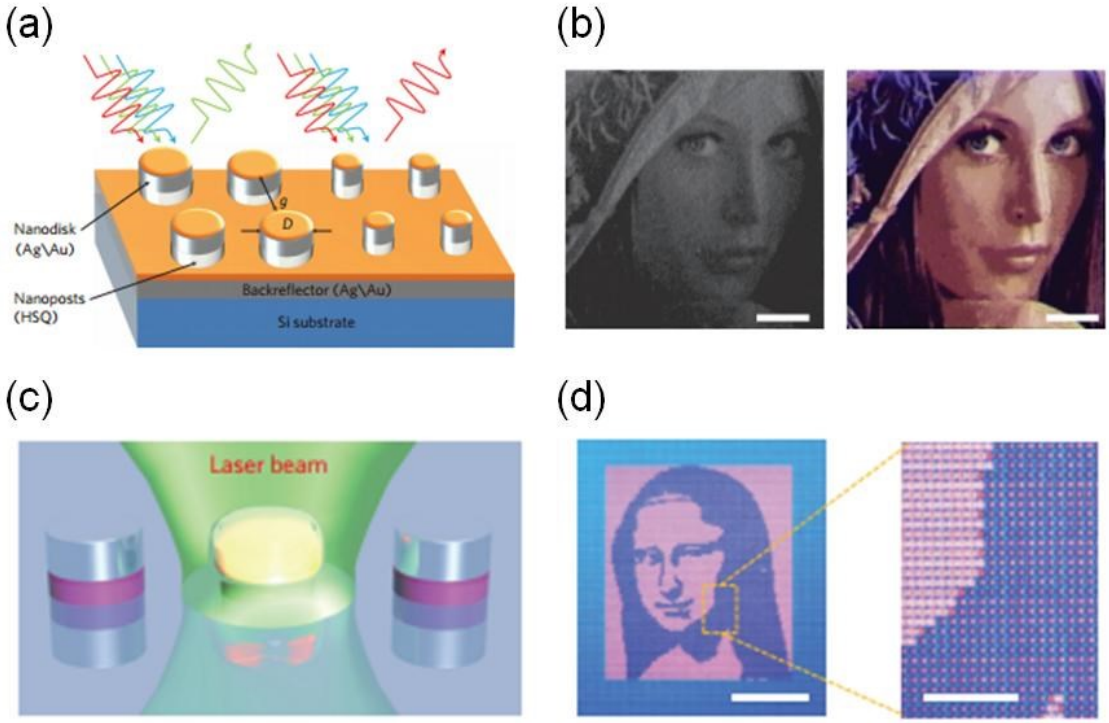

Figure 8. a) Interaction of white light with two closely spaced pixels, each consisting of four nanodisks. As a result of the different diameters (*D*) and separations (*g*) of the nanodisks within each pixel, different wavelengths of light are preferentially reflected back. b) Optical micrographs of the Lena image before (left) and after (right) metal deposition. Reproduced with permission.[101] Copyright 2012, Nature Publishing Group. c) A schematic illustration of laser printing. The printing is governed by photothermal reshaping of the metasurface. d) A printed portrait of Mona Lisa photographed by a camera with a macro lens. Scale bar: 2 mm. Inset shows a magnified image taken by a microscope exhibits colour dots with different dimensions. Scale bar: 500 µm. Reproduced with permission.[128] Copyright 2016, Nature Publishing Group.

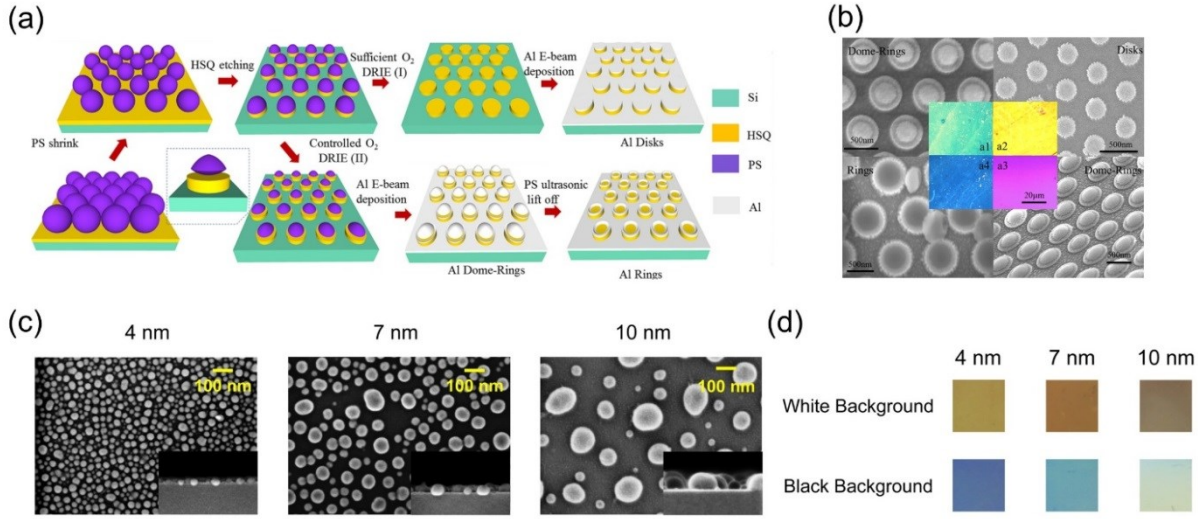

Figure 9. a) Schematic of the fabrication process of the Disks, Al Dome-Rings, and Rings, including hydrogen silsesquioxane (HSQ, Dow Corning XR-1541) spin coating and polystyrene (PS) monolayer transfer; PS size shrinkage; HSQ etching; removal of PS using two routes: route I, O_2 reactive-ion etching (RIE) process to completely remove the top PS and obtain the Disks; or route II, O_2 DRIE to further shrink the PS spheres to obtain Al Dome-Rings; Rings are obtained by ultrasonic removal of the PS from the Al Dome-Rings. b) SEM and corresponding optical microscope images showing corresponding colors for a1) Al Dome-Rings with (*P, R, r*) = (628, 250, 150 nm); a2) Disks with (*P, R, H*) = (420, 150, 60) nm; a3), Al Dome-Rings with (*P, R, r*) = (520, 200, 100 nm); a4) Rings with (*P, R, r*) = (628, 200, 100) nm. Reproduced with permission.[130] Copyright 2016, American Chemical Society. c) Sample SEM images for different initial silver ultrathin metal film thicknesses (i.e., before dewetting). d) Photographs for the three samples on white and black backgrounds. Reproduced with permission.[131] Copyright 2016, American Chemical Society.

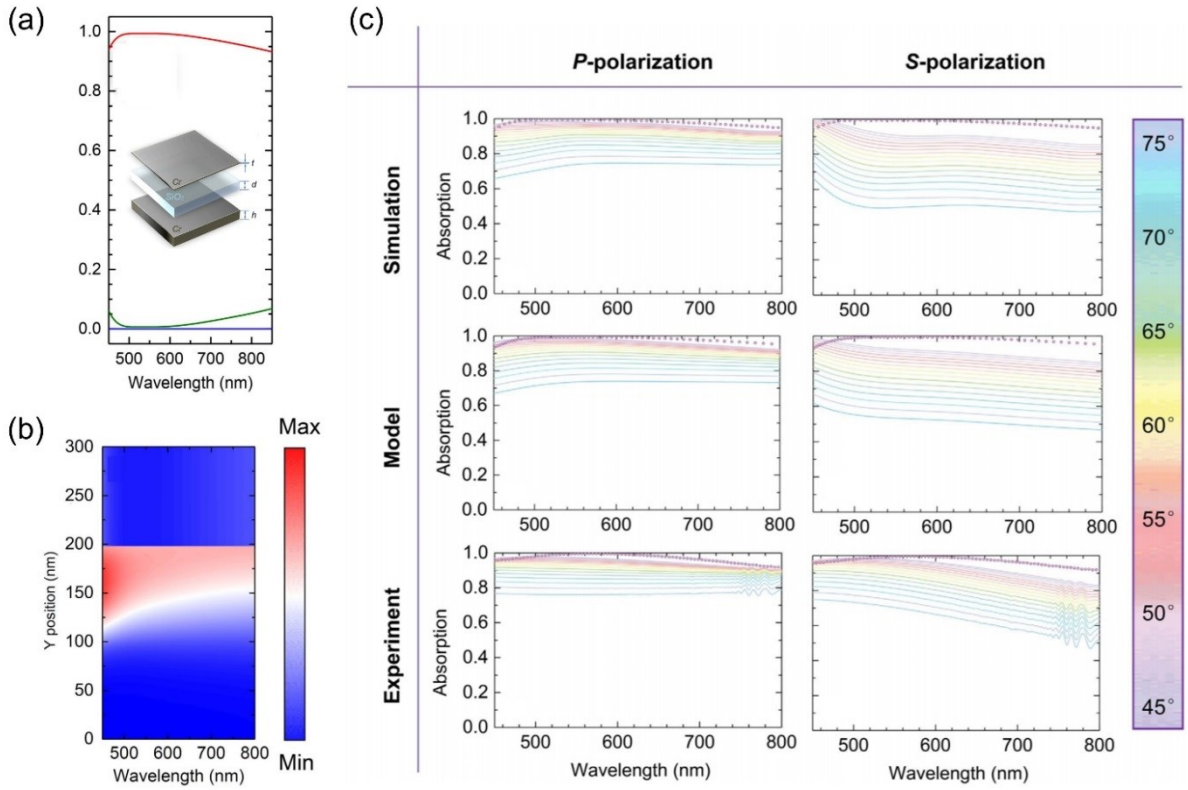

Figure 10. a) Simulated absorption and reflection spectra of a broadband MIM absorber employing lossy metals. Inset is the detailed schematic diagram with the thicknesses of top Cr, SiO_2, and bottm Cr being 3, 95, and 100 nm, respectively. b) Electrical field distribution inside this broadband absorber, presenting a weakly confined cavity. Three layers are located at 0-100 nm (bottom Cr), 100–195 nm (SiO_2), and 195-198 nm (top Cr), respectively, along the y axis. c) Simulated and measured angle resolved absorption of the absorber in (a) for both polarizations, showing an angle-independent absorption behavior up to 60°. Reproduced with permission.[152] Copyright 2015, Nature Publishing Group.

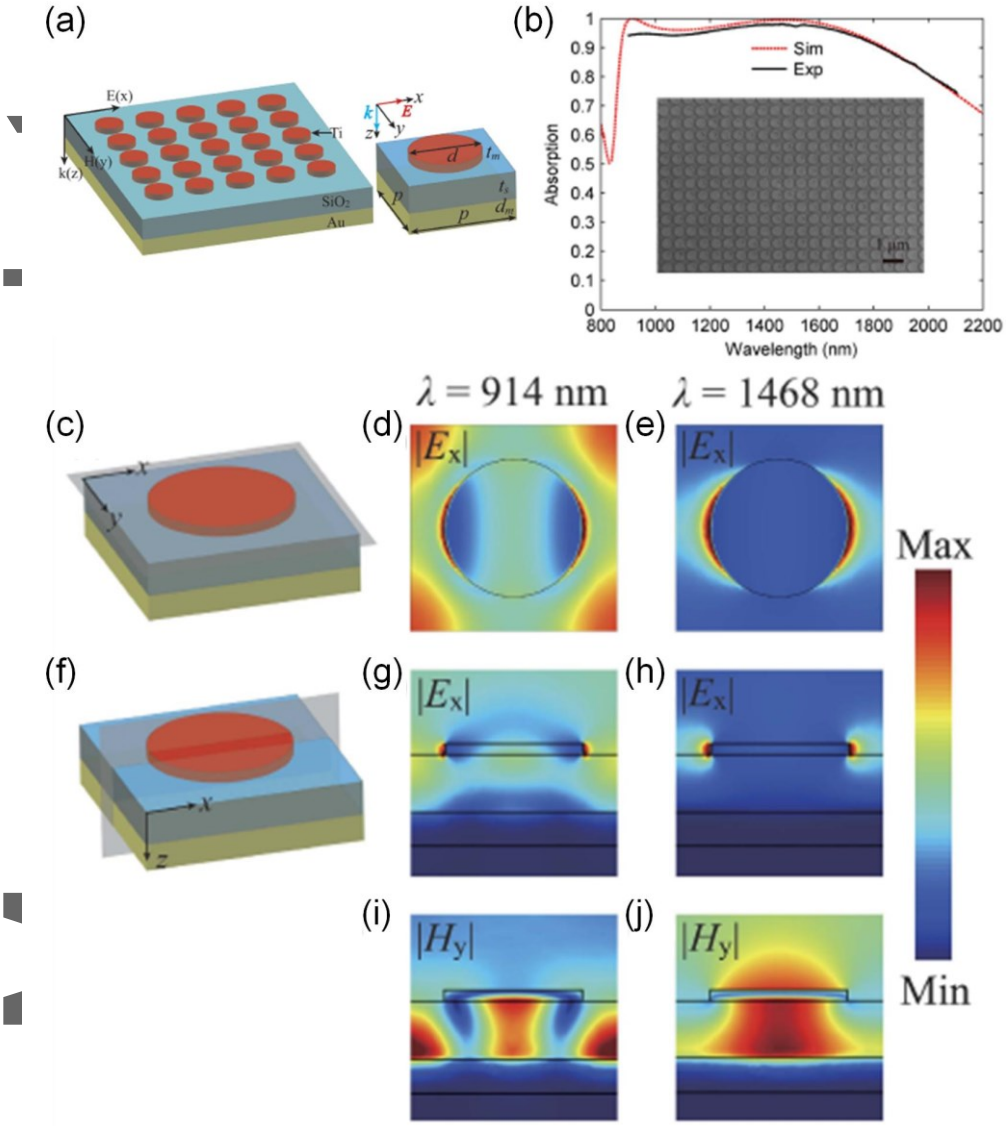

Figure 11. a) The schematic representation of the infrared broadband plasmonic absorber employing lossy Ti as the top metallic patterns with period (p) = 600 nm, thickness t_m = 30 nm, and diamter d = 400 nm. The thicknesses of the middle SiO_2 (t_s) and Au (d_m) are 160 nm and 100 nm, respectively. b) Simulated and measured absorption spectra of the designed absorber. Inset shows the SEM image of the fabricated sample with the scale bar of 1 µm. c–j) Normalized electric (E_x) and magnetic (H_y) field distributions in both x–y and x–z planes at two absorption peaks. Reproduced with permission.[153] Copyright 2016, Nature Publishing Group.

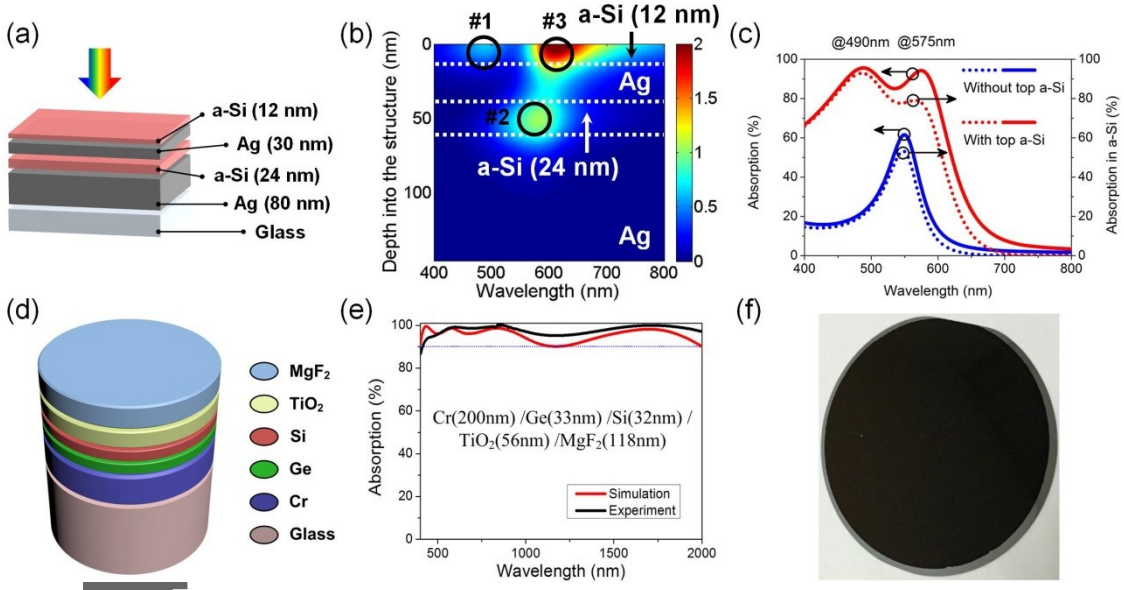

Figure 12. a) A schematic diagram of the broadband visible absorber employing multiple metal-semiconductor resonances. b) Electric field intensity distribution within the whole structure at all wavelengths. c) Simulated absorption of both metal-semiconductor-metal (MSM) and metal-semiconductor-metal-semiconductor (MSMS). It shows a broadened absorption by introducing additional resonances with the top a-Si layer. Reproduced with permission.[175] Copyright 2016, AIP Publishing LLC. d) Schematic of an ultra-broadband absorber featuring graded refractive index profile. e) Simulated and measured absorption spectra of this design, showing an average absorption >97% from 400 nm to 2 µm. f) Optical image of the fabricated absorber device under normal incidence. Reproduced with permission.[176] Copyright 2016, American Chemical Society.

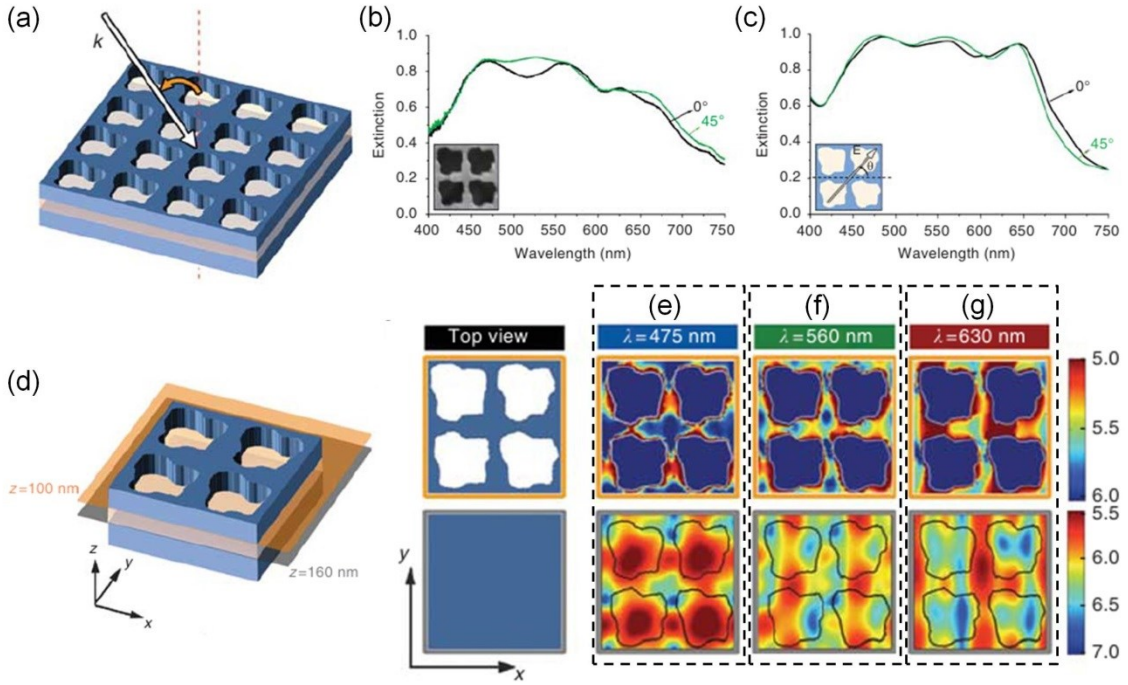

Figure 13. a) A schematic drawing of the 3D MIM metamaterial absorber with crossed trapezoid Ag arrays atop. b) Measured and c) simulated absorption spectra of the structure at two different polarization angles (ϑ = 0° and 45°), respectively. Inset in (b) shows the SEM image of the fabricated device, which is used for the simulation. Inset in (c) illustrates the polariztion angles. d–g) 2D (in *x*–*y* plane) absorption maps for three absorption peaks (as shown in (b) and (c)) at the planes between the top Ag/SiO_2 (orange plane) and SiO_2/bottom Ag (grey plane). Plots are displayed in the logarithmic scale and the red color refers to higher absorption. Reproduced with permission.[155] Copyright 2011, Nature Publishing Group.

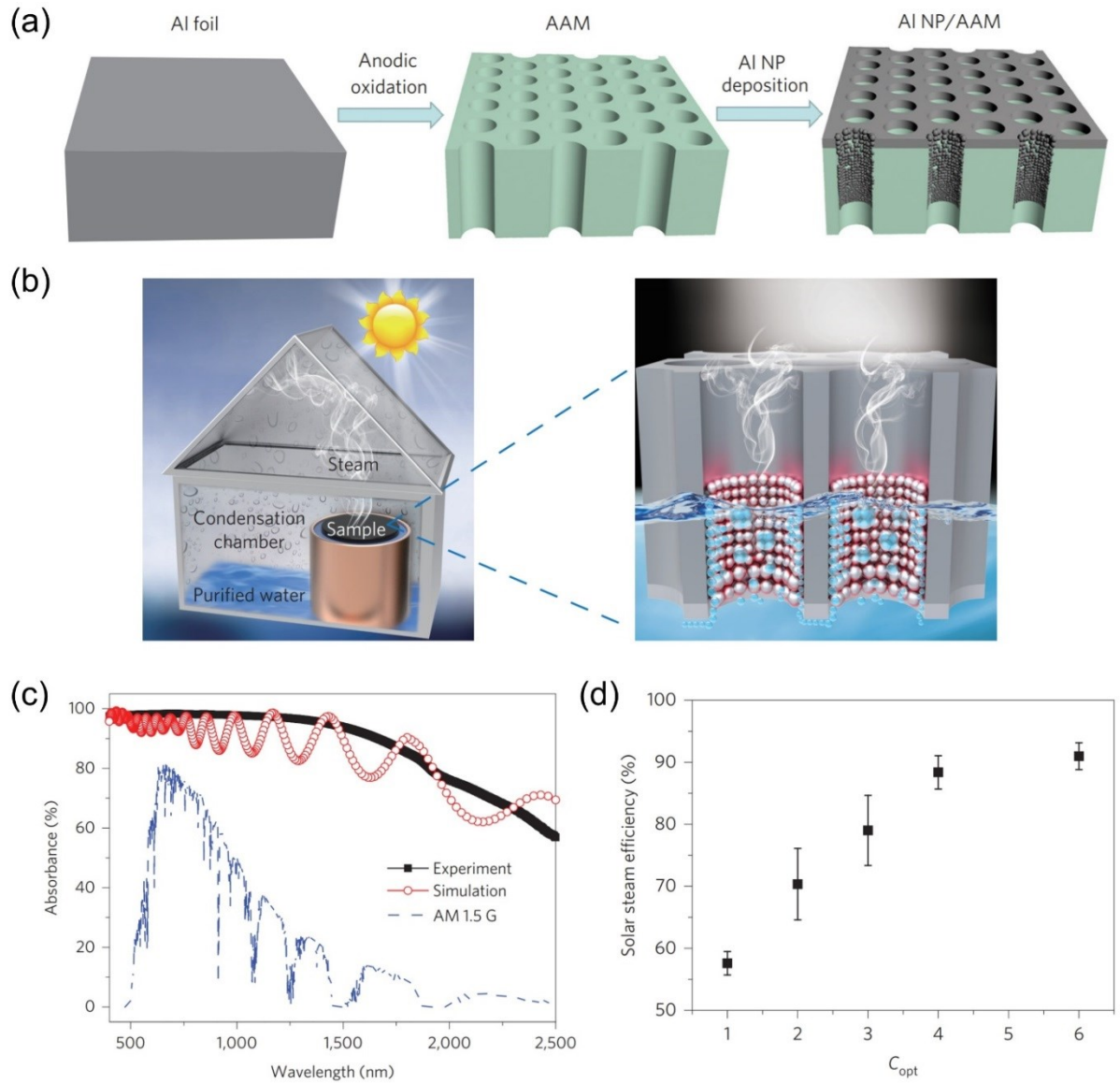

Figure 14. a) Fabrication process of the plasmon-enhanced broadband employing Al NPs. b) Solar desalination set-up. The porous AAM allows for both highly locallized heating and efficient water supply, thus resulting in effective steam generation and desalination. c) Measured and simulated absorption of plasmonic absorbers, showing great consistency with each other. The normalized spectra of solar light (AM1.5G, blue curve) clearly indicates that most of the solar energy gets absorbed by the plasmonic structures. d) Solar steam efficiency of the Al NP-based absorber for different values of C_{opt} (optical concentrations, e.g., C_{opt} = 4 refers to 4 sun illumination). The efficiency is defined as $\eta = mh_{LV} / C_{opt} P_0$ where m is the mass flux, h_{LV} is the latent enthalpy of the liquid-vapour phase change, and P_0 refers to the solar irradiation power of one sun (1 kW m^{-2}). Reproduced with permission.[187] Copyright 2016, Nature Publishing Group.

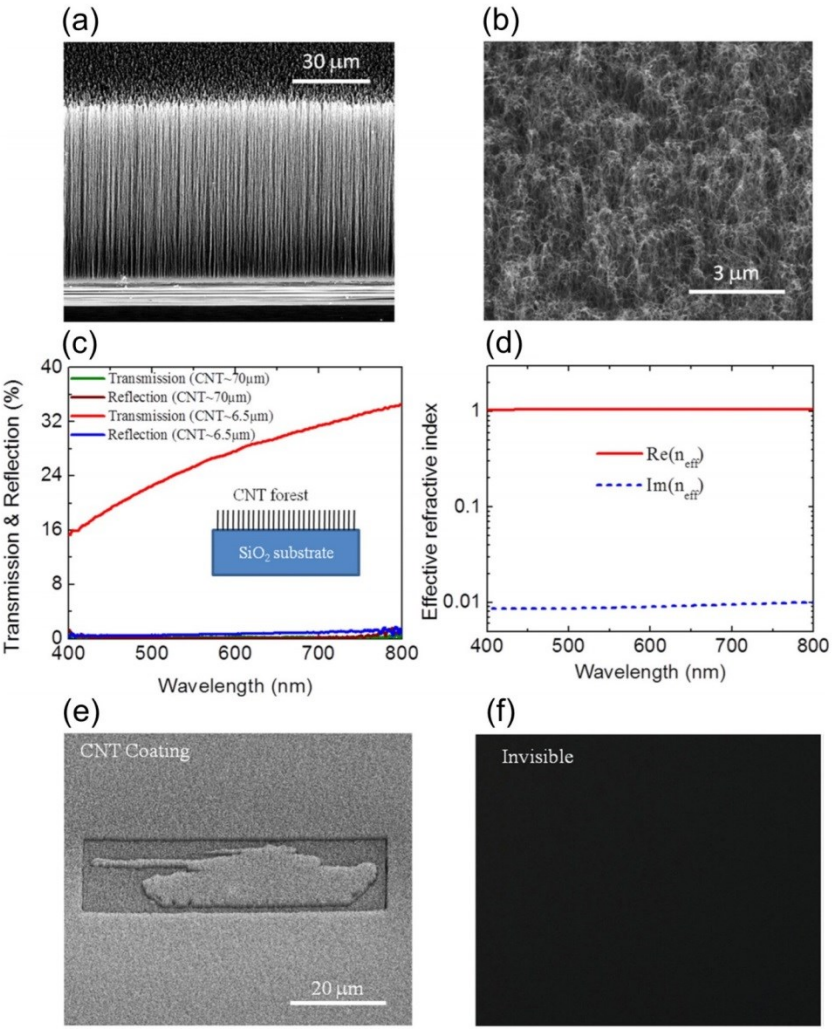

Figure 15. a,b) Cross section and top view SEM images of the CNT forest, respectively. c) Measured reflection and transmission spectra for 6.5 μm and 70 μm CNT on silica substrate. Incident light gets perfectly absorbed when the CNT is thick enough. d) Retrieved complex effective index of CNT forest over visible spectrum with the effective medium theory, indicating the perfect impedance match to the surrounding air. e) SEM image of the 'tank' pattern covered with 60 μm CNT coating. f) Optical image of the tank pattern under broadband visible illumination, showing that the pattern is totally invisible. Reproduced with permission.[195] Copyright 2011, AIP Publishing LLC.

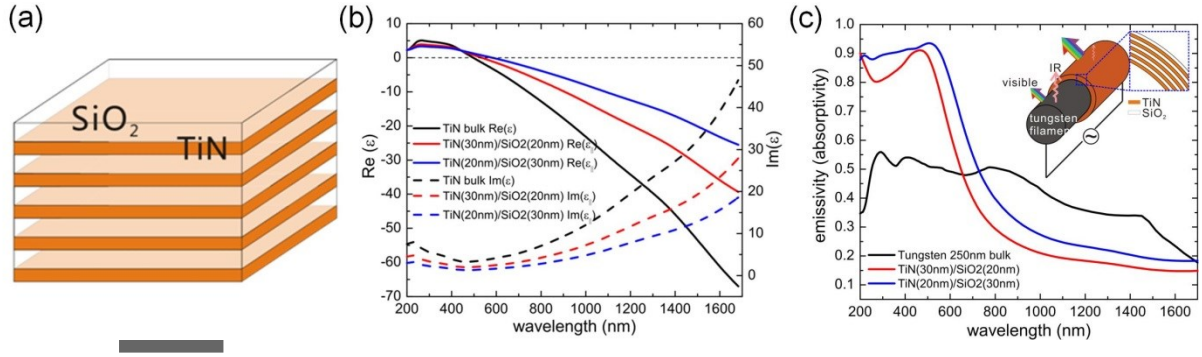

Figure 16. a) Schematic diagram of the broadband OTT absorber comprising alternating metal-dielectric multi-layers. Here, TiN is utilized as the metallic materials due to its high temperature stability. b) Wavelength dependent effective permittivity ($\varepsilon_{\parallel}$) of two stacks with different metal fill ratios. The permittivity of TiN is plotted for reference. c) Comparison of emissivity of tungsten and two OTT structures investigated in (b). Both effective media here consist of 5 cycles of TiN/SiO_2. Reproduced with permission.[207] Copyright 2016, John Wiley & Sons.

Table 1. Performance comparison of various types of structural color filters.

	F–P cavity resonances		Guided mode resonances	Surface plasmon resonances
	Lossless cavity	Lossy cavity		
Brightness	High	Low	High	High
Angular independence	Low (can be mitigated by high-index materials)	High	Low	High
Spatial resolution	Low	Low	High	High
Fabrication cost	Low	Low	High	High

Table 2. Pros and cons of broadband perfect absorbers achieved with various methods.

	Lossy materials	Multiple resonances	Broadband impedance matching
Advantages	High temperature stability	Absorption band flexibility	Broadband absorption
Disadvantages	No use in PVs	Complicated fabrication	Limited designs

Submitted to ADVANCED OPTICAL MATERIALS

Subwavelength nanostructures featuring extraordinary optical properties have received considerable research interest in the field of structural color filters and broadband perfect absorbers owing to their unique advantages over conventional counterparts. This review summarizes recent work in these areas with a detailed discussion of design principles, characteristic performances, implementation approaches, and practical applications, aiming to inspire further investigations in nanotechnology.

Nanostructured Optical Materials

C. Ji, K.-T. Lee, Ting Xu, J. Zhou, H. J. Park, and L. J. Guo*

Engineering Light at the Nanoscale: Structural Color Filters and Broadband Perfect Absorbers

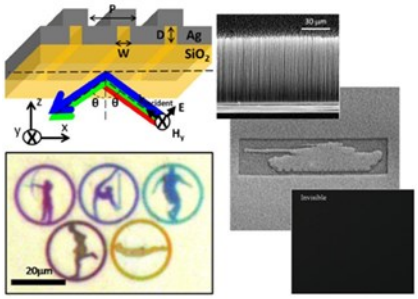

Submitted to ADVANCED OPTICAL MATERIALS

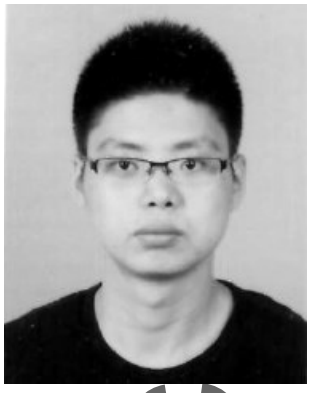

Chengang Ji received B.S. degree in optical information science and technology from Beijing Jiaotong University, China in 2013 and is currently a Ph.D. candidate in electrical engineering at the University of Michigan, Ann Arbor, MI, USA.

His research interests include nano and micro photonics, plasmonics, and optoelectronics.

Kyu-Tae Lee is a research scientist in Materials Research Department at Toyota Research Institute of North America. From 2015 to 2017, he was a postdoctoral research asscociate in Materials Science and Engineering at the University of Illinois, Urbana-Champaign. He received his Ph.D. degree in Electrical Engineering and Computer Science from the University of Michigan, Ann Arbor in 2015. His research interests include optics, optoelectronics, display, nanomaterials, and nanotechnology.

6161616161616161616161461616161

Submitted to ADVANCED OPTICAL MATERIALS

L. Jay Guo started his academic career with the University of Michigan in 1999, where he is currently a Professor of the Department of Electrical Engineering and Computer Science, with a joint appointment in Applied Physics, Mechanical Engineering, and Macromolecular Science and Engineering. He directs an interdisciplinary laboratory at the intersection of electrical engineering, photonics, polymer materials, and mechanical engineering. His group's research includes polymer-based photonic devices and sensor applications, organic and hybrid photovoltaics, plasmonic nanophotonics, and scalable nanomanufacturing technologies, such as roll-to-toll nanomanufacturing technologies.